

Article

The Influences of Different Parameters on the Static and Dynamic Performances of the Aerostatic Bearing

Jianbo Zhang ¹, Zhifang Deng ¹, Kun Zhang ¹, Hailiang Jin ^{1,*}, Tao Yuan ¹, Ce Chen ², Zhimin Su ¹, Yitao Cao ¹, Zhongliang Xie ³ , Danyang Wu ¹ and Jingping Sui ¹

¹ AECC Hunan Aviation Powerplant Research Institute, Zhuzhou 412002, China

² Army Aviation Institute, Beijing 101121, China

³ Department of Engineering Mechanics, Northwestern Polytechnical University, Xi'an 710072, China

* Correspondence: jin hailiang1984@gmail.com

Abstract: Aerostatic bearings have been widely applied to high-rotating speed machines due to their low friction and high rotational speed advantages. The geometry parameters, supply pressure and rotational speed play important roles in the static and dynamic performances of the aerostatic bearings. In this paper, the steady state and dynamic Reynolds equations are solved by the finite difference method (FDM) and used to study the static and dynamic performances of the aerostatic bearings. Then, combined with the motion equation of the rigid rotor-aerostatic bearing system, the linear stability of the aerostatic bearing is also studied. Moreover, based on the theory mentioned above, the influences of the geometry parameters (such as orifice diameter, radial clearance and eccentricity), rotational speed and supply pressure are investigated in detail. It was found that aerostatic bearing geometries, rotational speed and supply pressure had a significant effect on the steady and dynamic performances. Under the low-speed conditions and high supply pressure, the static pressure effect plays the main role in the performances of the aerostatic bearings, while on the contrary, the rotational effect plays the main role. Furthermore, a half-speed whirl may generate under certain conditions. The results also provide useful design guidelines for aerostatic bearings in high-speed machines.

Keywords: aerostatic bearing; static performance; dynamic coefficients; stability threshold; FDM



Citation: Zhang, J.; Deng, Z.; Zhang, K.; Jin, H.; Yuan, T.; Chen, C.; Su, Z.; Cao, Y.; Xie, Z.; Wu, D.; et al. The Influences of Different Parameters on the Static and Dynamic Performances of the Aerostatic Bearing. *Lubricants* **2023**, *11*, 130. <https://doi.org/10.3390/lubricants11030130>

Received: 6 November 2022

Revised: 7 February 2023

Accepted: 10 February 2023

Published: 13 March 2023



Copyright: © 2023 by the authors. Licensee MDPI, Basel, Switzerland. This article is an open access article distributed under the terms and conditions of the Creative Commons Attribution (CC BY) license (<https://creativecommons.org/licenses/by/4.0/>).

1. Introduction

With the merits of low noise, high precision, low friction, high rotational speed and long life, gas bearings have been widely applied in the high-precision and high-speed rotating machines, such as high-speed motors, ultra-precision machining spindles, precision guide rails and so on. Compared with traditional bearings like oil and ball bearings, gas bearings work with low heat generation, oil-free pollution and a simple auxiliary apparatus [1–6]. In order to overcome the poor load capacity of gas bearings due to the low viscosity, gas bearings with orifice restrictors, known as aerostatic bearings, use external high-pressure gas to generate extra load capacity. Like traditional oil bearings [7,8], water bearings [9,10] and squeeze film dampers [11,12], their static and dynamic characteristics are the key to their design and application, for which there exists numerous papers about the study of static and dynamic performances on them in the past. Similarly, in the application of the aerostatic bearings, the static and dynamic performance is also the key characteristic of the aerostatic bearings. In general, the static and dynamic characteristics contain the bearing capacity, static stiffness, dynamic stiffness and damping coefficient and linear stability. The static and dynamic characteristics of aerostatic bearings are affected by the geometry parameters and supply pressure of the aerostatic bearings and rotational speed, which leads to abundant literature on the characteristics of aerostatic bearings published in the past.

Cheng et al. [13] studied the effect of the number of orifices on the static performance of the aerostatic bearing and the results showed that the small number of feeding holes without locating the bearing bottom is suitable for a high-speed condition, while the large number of feeding holes is suitable for a low-speed condition. Ise et al. [14] researched the influence of the asymmetry supply pressure distribution of the upper and lower rows of orifices on the bearing capacity and mass flow of the aerostatic bearing. The results showed that this will lead to a larger bearing capacity with a decrease in the mass flow. The opening pressure-equalizing grooves were applied to improve the bearing capacity, while the effects of the parameters of the pressure-equalizing grooves on the bearing capacity and static stiffness were also studied [15]. Research showed that the opening pressure-equalizing grooves along the axis direction is more useful to the bearing capacity than the grooves along the circumferential direction. Su and Lie [16] investigated the rotational effect of the aerostatic bearing with orifices and a porous restrictor. The results showed that an aerostatic bearing with five rows of orifice feedings could match the porous air bearings in some certain characteristics, while the aerostatic bearings with orifices had less mass flow consumption. Moreover, the L/D (the ratio of bearing length to diameter) can be strengthened as the rotational effect. The influence of the orifice number and distribution on the static and dynamic performance was studied by Yang et al. [17] and the proper orifice distribution can eliminate the orifice backflow phenomenon. Wang et al. [18] studied the rotational effect on the static characteristics of a pure dynamic bearing, a pure aerostatic bearing and a hybrid gas bearing in detail. Moreover, they [19] also studied the effect of surface waviness along the axis and circumferential direction on the aerostatic bearings and the results showed that the bearing capacity, static stiffness and mass flow increased and the friction decreased with the increasing wave's amplitude.

As mentioned above, the static characteristics of the aerostatic bearings were studied by solving the steady state Reynolds equation, which ignores the squeezing effect. However, the gas film of aerostatic bearings is not only used for supporting and reducing friction and wear, but is also a key point of the bearing rotor system from the viewpoint of bearing rotordynamics. The performance of the gas film has an important effect on the dynamic performance of the gas-bearing rotor system. Therefore, the dynamic characteristics of the aerostatic bearings are also the key characteristic of the aerostatic bearings. Moreover, due to the compressibility and low viscosity of the gas, the aerostatic bearings tend to generate whirl instability under high rotational speed. Therefore, the linear stability of the aerostatic bearings is also an important property for the aerostatic bearings' application in high rotational speed machines.

Lund [20] adopted the linear Ph method to study whirl instability by the finite difference method (FDM), while Wadhwa et al. [21] also used the linear Ph method to investigate the effect of the rotational speed and geometry parameters on the dynamic stiffness, damping coefficient and the linear stability containing the critical rotational speed and mass. Han et al. [22] solved the dynamic Reynolds equation to obtain the dynamic stiffness and damping coefficients and then combined the rotor motion equation to obtain the orbit of the shaft center. The orbit of the shaft center obtained by numerical calculation was compared to the experimental results, which verified the correctness of the numerical calculation. Based on the research shown in reference [16], the stability of the aerostatic bearings with five rows of orifices and a porous restrictor was compared [23]. The whirl ratio was introduced into the study of dynamic stiffness and damping coefficients in references [17,24,25]. Chen et al. [24] found that static pressure effect plays the main role in the stability of the aerostatic bearing under the low rotational speed, while the rotational effect plays the main role in the stability under high speed. Moreover, the effect of different type of the orifice (i.e., inherent and simple orifice) on the stability was compared and the stability of the aerostatic bearing with an inherent orifice was better than the aerostatic bearing with a simple orifice under the same condition. Based on the gas flow state in the orifice by description of the Hagen–Poiseuille theory, a new Reynolds equation of aerostatic bearings was proposed to compute the dynamic coefficients. The stability threshold of the

aerostatic bearing-rotor system was investigated based on the modified Reynolds equation mentioned above. In the paper [17,20–26], the approach to obtain the dynamic coefficient is the same as Lund's [20] and the squeezing effect is not involved in the Reynolds equation directly in this study. By solving the transient Reynolds equation and motion equation of the rigid rotor, the stability of the aerostatic bearing with a single row and two rows of orifices was studied contrastively [27]. The results showed that the stability of the aerostatic bearing with two rows of orifices is better than the aerostatic bearing with a single row of orifices. Otsu et al. [28] considered the inertial effect of gas and investigated the stability of rigid rotor-aerostatic bearings with compound orifices and inherent orifices numerically and experimentally. The results presented that the compound orifices can improve the stability of the aerostatic bearing compared with the inherent orifices. Based the transfer function, Belforte et al. [29] proposed a new method to obtain the dynamic coefficients of a dynamic gas bearing analytically. Then, the method was used to obtain the dynamic coefficients of an aerostatic bearing [30]. Based on the study of the effect of surface waviness on the static performance of the aerostatic [19], Wang et al. [31] investigated the influence of surface waviness along the axis and circumferential direction on the dynamic coefficients of aerostatic bearings. In the same way, the effects of the waviness's amplitude and length on the dynamic coefficients were also studied. The research presented that the surface waviness has an obvious effect on the dynamic performance of aerostatic bearings. In addition, increasing the waviness's amplitude increases the dynamic coefficients.

To sum up, there exist numerous papers about the study of the static and dynamic performances of the aerostatic bearings. However, in this paper, the study of the static and dynamic performances of the aerostatic bearings focuses on some parameters' effects on the performances, which means that the study in this paper is detailed and comprehensive. In this paper, the steady and dynamic Reynolds equations for a linear aerostatic bearing-rotor system are solved to study the static performance, dynamic coefficients and linear stability. Moreover, the influences of the comprehensive parameters (such as eccentricity, rotational speed, gas film thickness, orifice diameter and supply pressure) on the static performance, dynamic coefficients and linear stability are also investigated in detail.

2. Mathematical Model

2.1. Reynolds Equation

The schematic diagram and coordinate axes of the aerostatic bearings are shown in Figure 1. There are two rows of inherent orifices, and each row contains eight feeding orifices distributed uniformly in the circumferential direction. In this paper, the Reynolds equation is used to calculate the gas pressure (p) distribution of the gas film. the Reynolds equation is shown in Equation (1) [3] and the gas film h can be calculated by Equation (2).

$$\frac{\partial}{\partial x} \left(p h^3 \frac{\partial p}{\partial x} \right) + \frac{\partial}{\partial z} \left(p h^3 \frac{\partial p}{\partial z} \right) = 6\eta u \frac{\partial(p h)}{\partial x} + 6\eta w \frac{\partial(p h)}{\partial x} + 12\eta \frac{\partial(p h)}{\partial t} - 12\delta \frac{\dot{m} p}{\rho dx dz} \quad (1)$$

$$h = c + e \cos(\varphi - \varphi_0) \quad (2)$$

where c is clearance; e is eccentricity; ρ is the density of the gas; φ_0 is the attitude angle at the mid plane; $z - L/2$ is the axial distance from the mid plane; Z_m is the mid plane; and

$$\delta = \begin{cases} 1, & \text{with orifices} \\ 0, & \text{without orifices} \end{cases}$$

$$\dot{m} = C_d \pi d_0 h p_s \sqrt{\frac{2\rho_a}{p_a}} \phi(p)$$

$$\phi(p) = \begin{cases} \left[\frac{\kappa}{2} \left(\frac{2}{\kappa+1} \right)^{\frac{\kappa+1}{\kappa-1}} \right]^{1/2}, & \frac{p}{p_s} \leq \left(\frac{2}{\kappa+1} \right)^{\frac{\kappa}{\kappa-1}} \\ \left\{ \frac{\kappa}{\kappa-1} \left[\left(\frac{p}{p_s} \right)^{\frac{2}{\kappa}} - \left(\frac{p}{p_s} \right)^{\frac{\kappa+1}{\kappa}} \right] \right\}^{1/2}, & \frac{p}{p_s} > \left(\frac{2}{\kappa+1} \right)^{\frac{\kappa}{\kappa-1}} \end{cases}$$

where δ is the Kronecker function; η is the dynamic viscosity of the gas; ρ_a is the gas density under atmosphere pressure; u is the circumferential velocity of the journal; w is the axial velocity of the journal; C_d is a discharge coefficient; κ is the heat capacity ratio; p_a is the atmospheric pressure; p_s is the supply pressure; and d_0 is the orifice diameter. When ignoring w , Equation (1) can be changed to Equation (3).

$$\frac{\partial}{\partial x} \left(ph^3 \frac{\partial p}{\partial x} \right) + \frac{\partial}{\partial z} \left(ph^3 \frac{\partial p}{\partial z} \right) = 6\eta u \frac{\partial(ph)}{\partial x} + 12\eta \frac{\partial(ph)}{\partial t} - 12\delta \frac{\dot{m}p}{\rho dx dz} \quad (3)$$

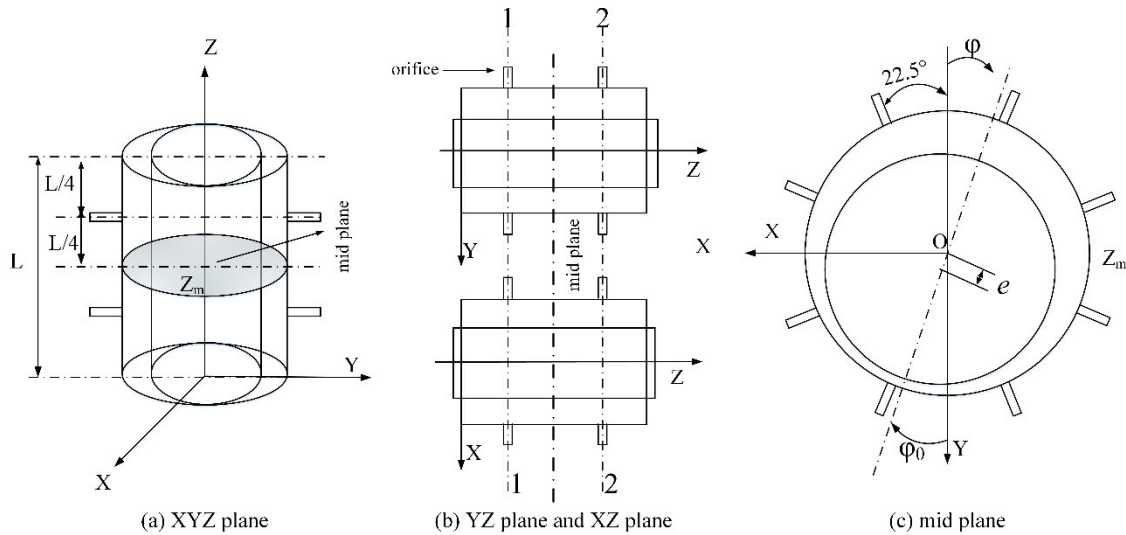


Figure 1. Schematic view of the aerostatic bearing: (a) XYZ plane; (b) YZ plane and XZ plane; (c) mid plane.

With the dimensionless parameters shown as below:

$$p = p_a P, h = cH, x = R\varphi, z = LZ, t = \frac{\tau}{\omega_s}, \lambda = \frac{\omega_s}{\omega}, \Lambda = \frac{6\eta\omega R^2}{p_a c^2}$$

(where ω_s is the journal perturbation rotational speed; ω is the rotational speed of the journal; λ is the whirl ratio; and Λ is the bearing number), Equation (3) can be changed to Equation (4).

$$\frac{\partial}{\partial \varphi} PH^3 \frac{\partial P}{\partial \varphi} + \left(\frac{R}{L} \right)^2 \frac{\partial}{\partial Z} PH^3 \frac{\partial P}{\partial Z} = \Lambda \frac{\partial}{\partial \varphi} (PH) + 2\Lambda\lambda \frac{\partial}{\partial \tau} (PH) + \delta Q_r \quad (4)$$

where $Q_r = -\frac{12\mu R}{c^3 L p_a \rho_a \Delta \varphi \Delta Z} \dot{m} = \Gamma_s \dot{m}$.

According to paper [14], the perturbed film thickness is

$$H = H_0 + H_X \Delta X + H_Y \Delta Y \quad (5)$$

where $H_X = \sin \varphi$ and $H_Y = \cos \varphi$. With the assumption that the X and Y components of the journal vibration are harmonic, the expression of the perturbed pressure is a complex form:

$$P = P_0 + P_X \Delta X + P_Y \Delta Y \quad (6)$$

where P_0 is the non-dimensional steady pressure and P_X, P_Y are the non-dimensional differential term of film pressure along the X and Y directions. The perturbed Q_r is:

$$Q_r = Q_{r0} + Q_{rY} \Delta Y + Q_{rX} \Delta X \quad (7)$$

where Q_{rY} and Q_{rX} are listed in the Appendix A. Then, with Equations (5)–(7), Equation (4) can yield the following perturbed Reynolds equations, shown in Equations (8)–(10).

$$\frac{\partial}{\partial \varphi} \left(P_0 H_0^3 \frac{\partial P_0}{\partial \varphi} \right) + \left(\frac{R}{L} \right)^2 \frac{\partial}{\partial Z} \left(P_0 H_0^3 \frac{\partial P_0}{\partial Z} \right) = \Lambda \frac{\partial}{\partial \varphi} (P_0 H_0) + \delta Q_{r0} \tag{8}$$

$$\begin{aligned} & \frac{\partial}{\partial \varphi} \left(P_0 H_0^3 \frac{\partial P_X}{\partial \varphi} + 3P_0 H_0^2 H_X \frac{\partial P_0}{\partial \varphi} + H_0^3 P_X \frac{\partial P_0}{\partial \varphi} \right) + \\ & \left(\frac{R}{L} \right)^2 \frac{\partial}{\partial \varphi} \left(P_0 H_0^3 \frac{\partial P_X}{\partial Z} + 3P_0 H_0^2 H_X \frac{\partial P_0}{\partial Z} + H_0^3 P_X \frac{\partial P_0}{\partial Z} \right) \\ & = \Lambda \frac{\partial}{\partial \varphi} (P_0 H_X + P_X H_0) + 2\Lambda \lambda i (P_0 H_X + P_X H_0) + \delta Q_{rX} \end{aligned} \tag{9}$$

$$\begin{aligned} & \frac{\partial}{\partial \varphi} \left(P_0 H_0^3 \frac{\partial P_Y}{\partial \varphi} + 3P_0 H_0^2 H_Y \frac{\partial P_0}{\partial \varphi} + H_0^3 P_Y \frac{\partial P_0}{\partial \varphi} \right) + \\ & \left(\frac{R}{L} \right)^2 \frac{\partial}{\partial \varphi} \left(P_0 H_0^3 \frac{\partial P_Y}{\partial Z} + 3P_0 H_0^2 H_Y \frac{\partial P_0}{\partial Z} + H_0^3 P_Y \frac{\partial P_0}{\partial Z} \right) \\ & = \Lambda \frac{\partial}{\partial \varphi} (P_0 H_Y + P_Y H_0) + 2\Lambda \lambda i (P_0 H_Y + P_Y H_0) + \delta Q_{rY} \end{aligned} \tag{10}$$

By adopting FDM, i.e., the finite difference method, Equations (8)–(10) can be changed into Equation (11) to Equation (13), and their computational domain is presented in Figure 2.

$$A_{0i,j} P_{0i+1,j}^2 + B_{0i,j} P_{0i-1,j}^2 + C_{0i,j} P_{0i,j+1}^2 + D_{0i,j} P_{0i,j-1}^2 - E_{0i,j} P_{0i,j}^2 = \Lambda \Delta \varphi (P_{0i+1,j} H_{0i+1,j} - P_{0i+1,j} H_{0i-1,j}) + (\Delta \varphi)^2 Q_{r0} \tag{11}$$

$$A_{Xij} P_{Xi+1,j} + B_{Xij} P_{Xi-1,j} + C_{Xij} P_{Xi,j+1} + D_{Xij} P_{Xi,j-1} + E_{Xij} P_{Xi+1,j} = F_{Xij} \tag{12}$$

$$A_{Yij} P_{Yi+1,j} + B_{Yij} P_{Yi-1,j} + C_{Yij} P_{Yi,j+1} + D_{Yij} P_{Yi,j-1} + E_{Yij} P_{Yi+1,j} = F_{Yij} \tag{13}$$

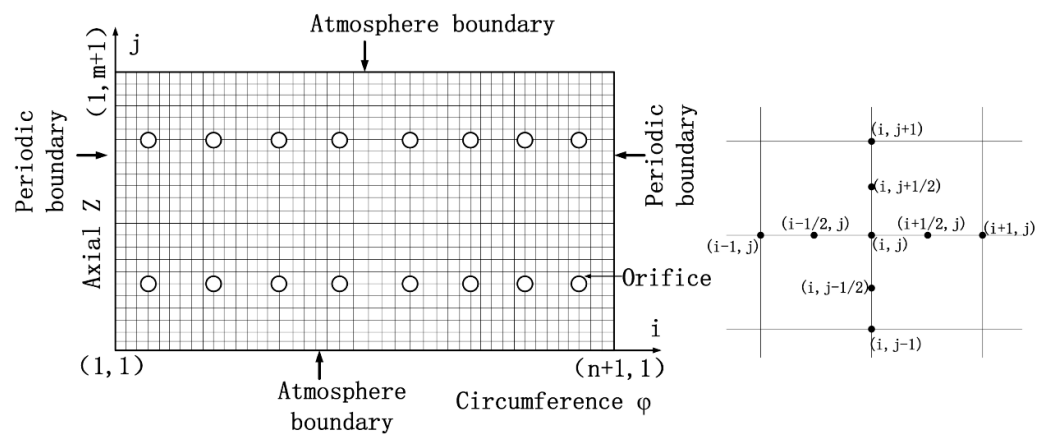


Figure 2. Computational domain of the Reynolds equation and grid structure.

2.2. Static Characteristics

By solving Equation (11), the pressure distribution of the gas film is obtained and then the load capacity W_X, W_Y along the X and Y directions is acquired by Equation (14), while the total load capacity is calculated by Equation (15) [32].

$$\begin{cases} W_X = - \int_0^L \int_0^{2\pi R} (p_0 - p_a) \sin \varphi dx dz \\ W_Y = - \int_0^L \int_0^{2\pi R} (p_0 - p_a) \cos \varphi dx dz \end{cases} \tag{14}$$

$$W = \sqrt{W_X^2 + W_Y^2} \tag{15}$$

As the load direction is the Y direction, $W_X = 0$ and we can calculate the correction of the attitude angle $\Delta\varphi$ by Equation (16).

$$\Delta\varphi = \tan^{-1}\left(\frac{W_X}{W_Y}\right) \tag{16}$$

In the end, the attitude angle φ_0 can be calculated through the iterative procedure, i.e., $\varphi_{new} = \varphi_{old} - \Delta\varphi$ until $\Delta\varphi = \frac{W_X}{W_Y} \leq 10^{-5}$, which means the load direction is the Y direction. After obtaining the bearing capacity, the static stiffness is given as:

$$K_w = \frac{dW}{de} \approx \frac{\Delta W}{\Delta e} = \frac{\Delta W}{c\Delta\varepsilon} \tag{17}$$

2.3. Dynamic Coefficients

Based on the solution of the steady-state Reynolds equation, i.e., Equation (11), the eight dynamic coefficients can be calculated by the solutions of Equations (12) and (13) and the eight dynamic coefficients can be calculated as follows:

$$\begin{cases} k_{xx} = -\frac{p_a RL}{c} \int_0^1 \int_0^{2\pi} Re(P_X) \sin(\varphi) d\varphi dZ \\ k_{yx} = -\frac{p_a RL}{c} \int_0^1 \int_0^{2\pi} Re(P_X) \cos(\varphi) d\varphi dZ \\ k_{yy} = -\frac{p_a RL}{c} \int_0^1 \int_0^{2\pi} Re(P_Y) \cos(\varphi) d\varphi dZ \\ k_{xy} = -\frac{p_a RL}{c} \int_0^1 \int_0^{2\pi} Re(P_Y) \sin(\varphi) d\varphi dZ \\ c_{xx} = -\frac{p_a RL}{c\omega} \int_0^1 \int_0^{2\pi} Im(P_X) \sin(\varphi) d\varphi dZ \\ c_{yx} = -\frac{p_a RL}{c\omega} \int_0^1 \int_0^{2\pi} Im(P_X) \cos(\varphi) d\varphi dZ \\ c_{yy} = -\frac{p_a RL}{c\omega} \int_0^1 \int_0^{2\pi} Im(P_Y) \cos(\varphi) d\varphi dZ \\ c_{xy} = -\frac{p_a RL}{c\omega} \int_0^1 \int_0^{2\pi} Im(P_Y) \sin(\varphi) d\varphi dZ \end{cases} \tag{18}$$

2.4. Whirl Instability Analysis

The rigid rotor-aerostatic bearings are shown in Figure 3 and the two rotor ends are supported by aerostatic journal bearings, while the rotor mass is $2m_r$ and contains zero unbalanced mass. When the journal is disturbed by tiny dynamic excitations with whirl speed ω_s , the gas film force ΔF_X , ΔF_Y can be written as Equation (19) and the motion equation is shown as Equation (20).

$$\begin{cases} \Delta F_X = k_{xx}\Delta x + k_{xy}\Delta y + c_{xx}\Delta\dot{x} + c_{xy}\Delta\dot{y} \\ \Delta F_Y = k_{yy}\Delta y + k_{yx}\Delta x + c_{yy}\Delta\dot{y} + c_{yx}\Delta\dot{x} \end{cases} \tag{19}$$

$$\begin{cases} m_r\ddot{x} + \Delta F_X = 0 \\ m_r\ddot{y} + \Delta F_Y = 0 \end{cases} \tag{20}$$

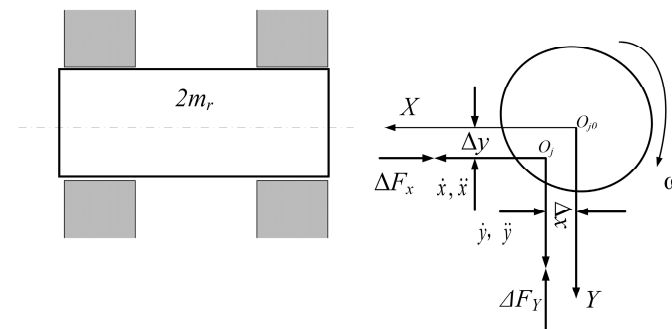


Figure 3. Rigid rotor and aerostatic journal bearing system.

Substituting Equation (21)

$$\begin{cases} \Delta x = x_0 e^{i\omega_s t} \\ \Delta y = y_0 e^{i\omega_s t} \end{cases} \quad (21)$$

where x_0 and y_0 are the constant, into Equation (20), Equation (22) can be obtained, where the k_{eq} is inertial force and is equal to $m_r \omega_s^2$.

$$\begin{cases} \Delta F_X = k_{eq} x_0 e^{i\omega_s t} \\ \Delta F_Y = k_{eq} y_0 e^{i\omega_s t} \end{cases} \quad (22)$$

With Equations (19) and (21), Equation (22) can be rewritten as:

$$\begin{cases} (k_{xx} - k_{eq} + ic_{xx}\omega_s)x_0 + (k_{xy} + ic_{xy}\omega_s)y_0 = 0 \\ (k_{yx} + ic_{yx}\omega_s)x_0 + (k_{yy} - k_{eq} + ic_{yy}\omega_s)y_0 = 0 \end{cases} \quad (23)$$

As $x_0 \neq 0$, $y_0 \neq 0$, Equation (24) can be obtained as follows and then rewritten as Equation (25).

$$\begin{vmatrix} k_{xx} - k_{eq} + ic_{xx}\omega_s & k_{xy} + ic_{xy}\omega_s \\ k_{yx} + ic_{yx}\omega_s & k_{yy} - k_{eq} + ic_{yy}\omega_s \end{vmatrix} = 0 \quad (24)$$

$$\begin{cases} (k_{xx} - k_{eq})(k_{yy} - k_{eq}) - k_{yx}k_{xy} - c_{xx}c_{yy}\omega_s^2 + c_{yx}c_{xy}\omega_s^2 = 0 \\ (k_{xx} - k_{eq})c_{yy}\omega_s + (k_{yy} - k_{eq})c_{xx}\omega_s - (k_{yx}c_{xy}\omega_s + k_{xy}c_{yx}\omega_s) = 0 \end{cases} \quad (25)$$

By adopting the dimensionless parameters:

$$\begin{aligned} K_{xx} &= \frac{c}{p_a RL} k_{xx}; K_{xy} = \frac{c}{p_a RL} k_{xy}; K_{yx} = \frac{c}{p_a RL} k_{yx}; K_{yy} = \frac{c}{p_a RL} k_{yy} \\ C_{xx} &= \frac{c\omega}{p_a RL} c_{xx}; C_{xy} = \frac{c\omega}{p_a RL} c_{xy}; C_{yx} = \frac{c\omega}{p_a RL} c_{yx}; C_{yy} = \frac{c\omega}{p_a RL} c_{yy} \\ \bar{M} &= \frac{m_c \omega^2}{p_a RL}; (K_{eq})_c = (\bar{M} \lambda^2)_c \end{aligned}$$

Equation (25) can be rewritten as:

$$\begin{cases} (K_{xx} - K_{eq})(K_{yy} - K_{eq}) - K_{yx}K_{xy} - (C_{xx}C_{yy} - C_{yx}C_{xy})\gamma^2 = 0 \\ (K_{xx} - K_{eq})C_{yy} + (K_{yy} - K_{eq})C_{xx} - (K_{yx}C_{xy} + K_{xy}C_{yx}) = 0 \end{cases} \quad (26)$$

In the end, we can obtain the critical whirl ratio λ_c and critical non-dimensional inertial force $(K_{eq})_c$ by using Equation (27).

$$\begin{cases} \lambda_c^2 = \frac{(K_{xx} - (K_{eq})_c)(K_{yy} - (K_{eq})_c) - K_{yx}K_{xy}}{C_{xx}C_{yy} - C_{yx}C_{xy}} \\ (K_{eq})_c = \frac{-K_{yx}C_{xy} - K_{xy}C_{yx} + K_{xx}C_{yy} + K_{yy}C_{xx}}{C_{xx} + C_{yy}} \end{cases} \quad (27)$$

2.5. The Flow Chart of the Solution of the Reynolds Equations

As shown in Figure 4, with the calculation parameters (i.e., geometry parameters of bearing, supply pressure and rotation speed), the steady Reynolds equation (i.e., Equation (11)) is solved until there is convergence of the steady-state pressure and $|W_x/W_y| \leq 10^{-5}$. Based on the solution of Equation (11), the dynamic Reynolds equation (i.e., Equations (12) and (13)) is solved until there is convergence of the perturbed pressure (i.e., P_x and P_y) with the initial whirl ratio λ . Then, the dynamic coefficients can be calculated by Equation (18) and the critical whirl ratio is obtained by Equation (27) with the dynamic coefficients until there is convergence of λ_c and λ by the iteration solution of coupled Equations (12), (13) and (27). When the convergence of λ_c and λ is verified, the stability thresholds of both the critical whirl ratio and the critical inertial force are obtained.

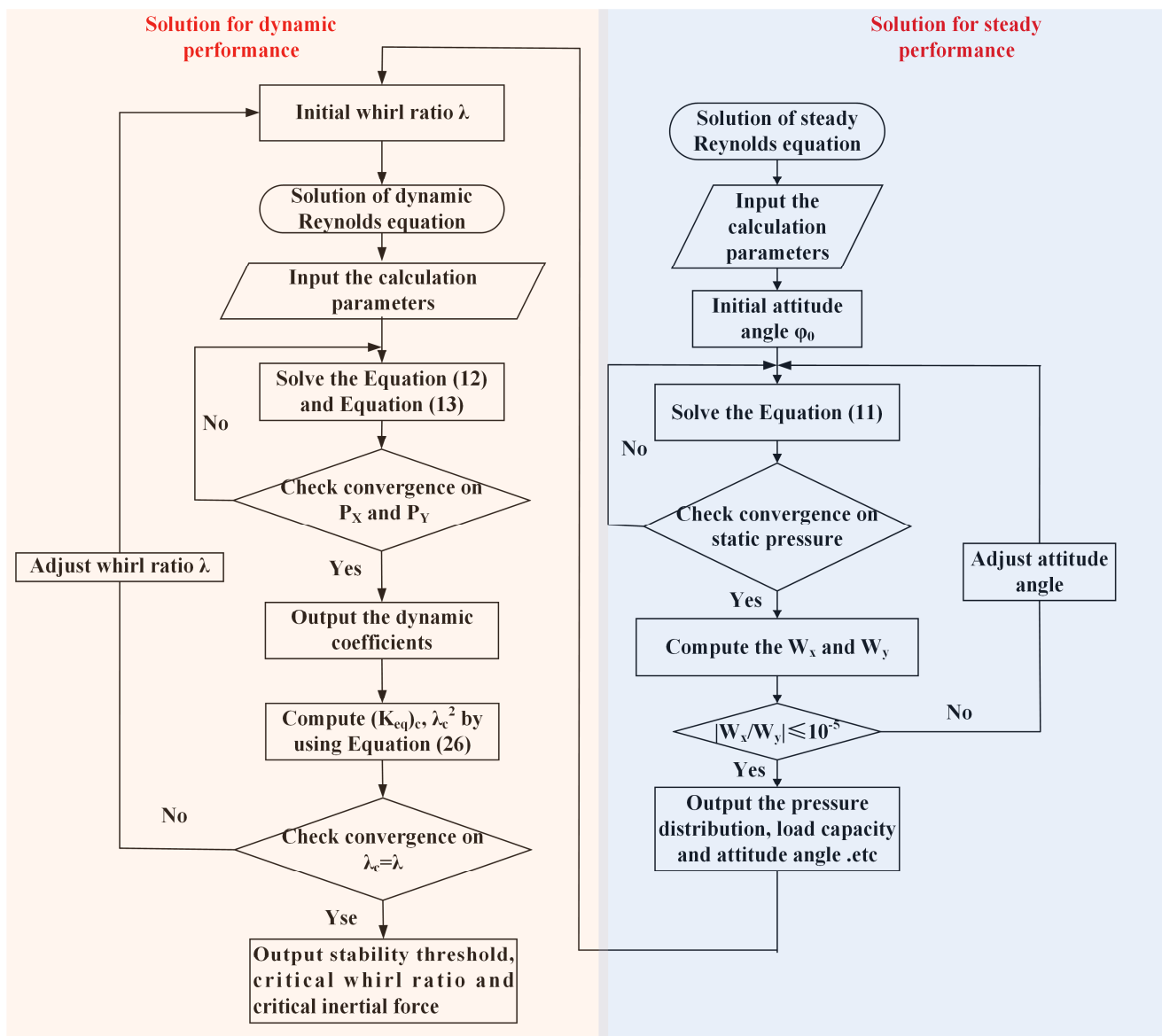


Figure 4. Flow chart of the solution of the critical whirl ratio and the critical inertial force.

2.6. The Verification of the Solution for the Reynolds Equation

In order to verify the correctness of the numerical method, the results obtained from the present research were compared with the results from the paper [33]. The comparison of the calculation parameters are the same to the parameters in the paper [33]. The results calculated by the present study and published paper [33] are shown in Figure 5. As shown in the figure, the results from the present study show good agreement with the results from that of paper [33], which indicates the correctness of the calculation method in this paper. The load capacities with different mesh numbers of m and n are shown as follows. In order to select the appropriate number of grids, the load capacities with different mesh numbers of m and n are shown in Table 1. The aerostatic bearings' parameters used in this section can be seen in the Table 2. The results show that when the number of grids increases to a certain value, the change of the bearing capacity is not obvious. In order to ensure calculation efficiency, the selected number of grids is $m = 64$, $n = 96$.

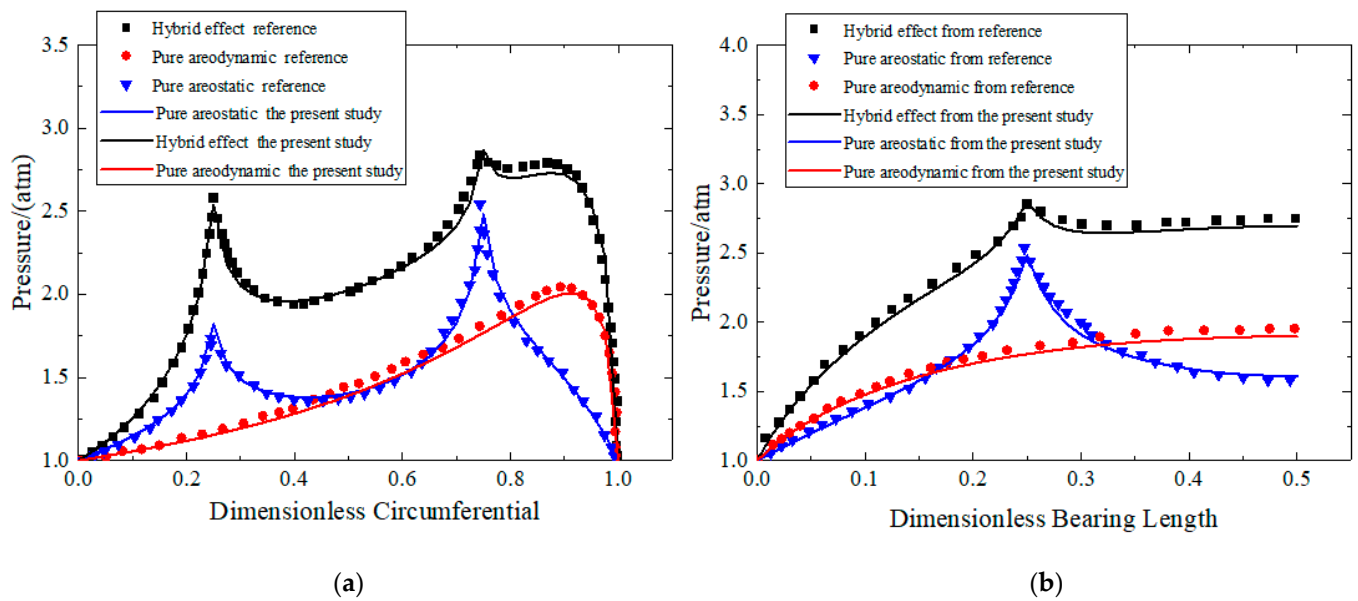


Figure 5. The pressure distribution from the presented study and published paper [33]: (a) pressure distribution along with the circumferential direction; (b) pressure distribution along with the axial direction.

Table 1. The calculation results with different numbers of m and n .

The Number of m	The Number of n	Load Capacity/ N
16	32	177.33
32	32	174.80
32	64	173.23
48	80	171.67
64	96	171.15
64	128	170.83

Table 2. The calculation parameters used in this section.

Calculation Parameters	Value
Bearing diameter (D)	25 mm
Bearing length (L)	50 mm
Gas density (ρ)	1.204 kg/m ³
Gas viscosity (η)	1.82·10 ⁻⁵ Ns/m ²
Ration of specific heat of gas (κ)	1.4
Atmospheric pressure (atm) (p_a)	101,325 Pa
Rows of the orifice	2
The orifice number of each row orifice	8

3. Results and Discussion

In this section, the influences of the different parameters (such as rotational speed, eccentricity, gas film thickness, orifice diameter and supply pressure) on the static performances are studied by solving the steady state Reynolds equation first. Then, the effects of the different parameters on the dynamic coefficients and stability are investigated by solving the dynamic Reynolds equation and rigid rotor motion equations in detail.

3.1. Static Performances

In this section, according to the Section 2 theory and method, the influences of different parameters on the static performances (such as bearing capacity, static stiffness, attitude angle and so on) are studied as follows. The aerostatic bearings' parameters used in this section can be seen in Table 2.

3.1.1. The Influences of Rotational Speed and Eccentricity

In this section, the reference parameters are $d_0 = 0.2$ mm, $p_s = 7$ atm, $c = 15$ μ m and the variable parameters are eccentricity and rotational speed. Figures 6–8 describe the effects of the eccentricity and rotational speed on the bearing capacity, static stiffness and attitude angle. As shown in Figure 6, under a certain rotational speed, the bearing capacity increases with increasing eccentricity. The reason is as follows: with zero speed, the aerostatic bearing is under the pure static state and the gas film thickness of the upper half increases with an increase in the eccentricity, which leads to a decrease in the pressure of the orifice. On the contrary, the gas film thickness of the lower half decreases with the increasing eccentricity and the pressure of the orifice increases. The decreasing of the upper half and the increasing of the lower half results in the growth of the bearing capacity. When the rotational speed is not zero, the aerostatic bearing is under the hybrid state. With increasing eccentricity, on one hand, the gap of the pressure of the orifices at the upper and lower halves becomes larger; on the other hand, the rotational effect will be strengthened. This will increase the bearing capacity when the eccentricity increases. Moreover, under a certain the eccentricity, the bearing capacity increases with the increase of the speed, as the rotational effect is strengthened. When the eccentricity is larger, the rotational speed effect is more obvious.

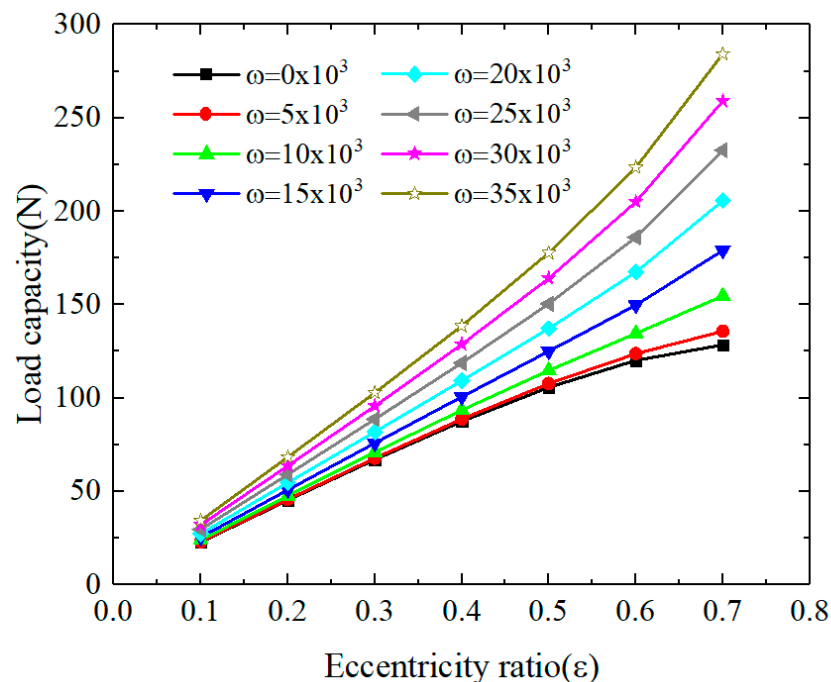


Figure 6. The effects of the eccentricity ratio and rotational speed on the load capacity (reference parameters: $d_0 = 0.2$ mm, $p_s = 7$ atm, $c = 15$ μ m).

As shown in Figure 7, the static stiffness decreases with the increasing eccentricity under the lower rotational speed (such as zero or 5000 rpm). According to Equation (17), the stiffness is the first derivative of the load capacity to eccentricity. As shown in Figure 6, under lower speed conditions, the slope of the load capacity decreases with an increase of ϵ for a certain speed. Therefore, as shown in Figure 7, under a lower speed condition, the stiffness decreases with an increase of ϵ for a certain speed. However, as shown in Figure 6, under hybrid conditions, the slope of the load capacity increases with an increase of ϵ for a certain speed. Therefore, under hybrid conditions, the stiffness increases with an increase of ϵ for a certain speed. Moreover, the static stiffness increases with the increasing rotational speed, which is caused by the strengthening rotational effect.

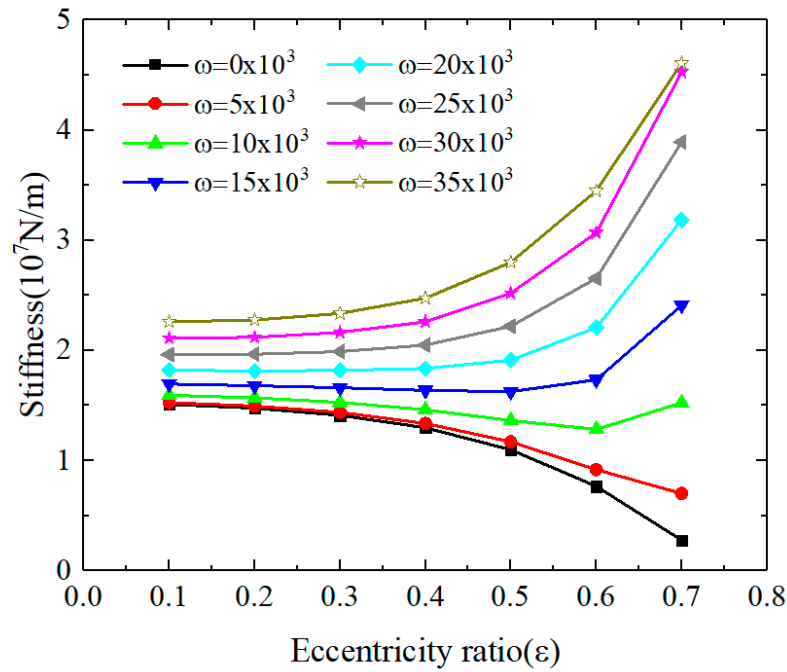


Figure 7. The effects of the eccentricity ratio and rotational speed on the steady stiffness (reference parameters: $d_0 = 0.2$ mm, $p_s = 7$ atm, $c = 15$ μm).

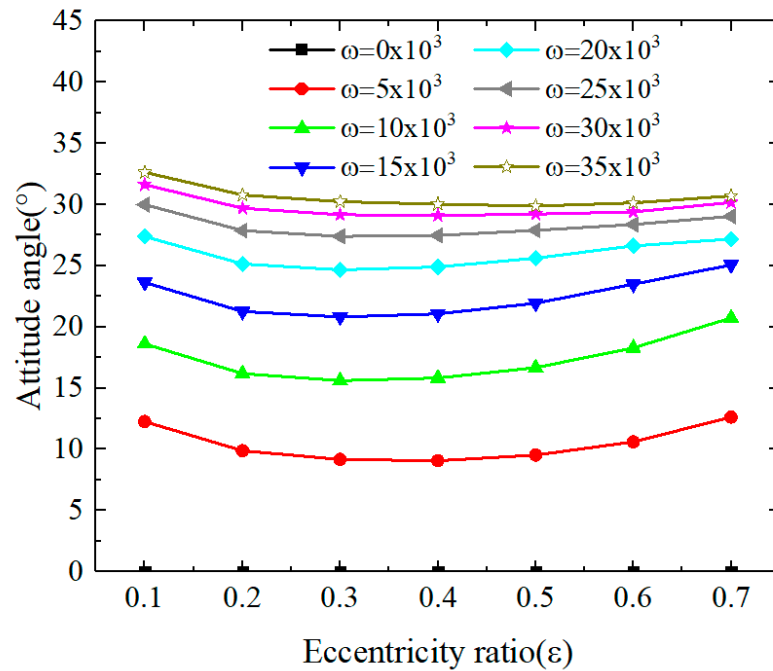


Figure 8. The effects of the eccentricity ratio and rotational speed on the attitude angle (reference parameters: $d_0 = 0.2$ mm, $p_s = 7$ atm, $c = 15$ μm).

As shown in Figure 8, for a certain speed, the attitude angle decreases slightly and then increases with the increase of eccentricity. On the whole, the attitude angle does not change significantly with the eccentricity. Moreover, the attitude angle is almost zero under a pure-static condition, which meets the theory and verifies the correctness of the method in the paper. For certain eccentricity, the attitude angle increases with the increasing speed and the slope of the attitude angle decreases with the increasing speed.

3.1.2. The Influences of Gas Film Radial Clearance

In this section, the reference parameters are $d_0 = 0.2$ mm, $p_s = 7$ atm, $\varepsilon = 0.4$ and the variable parameters are the radial clearance and rotational speed. Figures 9–11 describe the effects of the radial clearance on the bearing capacity, static stiffness and attitude angle. As shown in Figures 9 and 10, under the pure-static condition, the bearing capacity and stiffness increase and then decrease with the increase of the radial clearance, while the bearing capacity and stiffness decrease with the increase of the radial clearance under the higher speed. Under the pure-static condition, for a certain eccentricity, the pressure differential of the upper and lower halves of the aerostatic bearings increases with an increase of the radial clearance at the small radial clearance, which results in the increase of the bearing capacity. However, at the bigger radial clearance, the pressure differential of the upper and lower halves of the aerostatic bearings decreases with increase of the radial clearance, which results in the decrease of the bearing capacity. When the rotational speed is high, the aerostatic bearing is under the hybrid state and the bearing capacity is obviously affected by the rotational effect. Therefore, the rotational effect weakens with an increase of the radial clearance, which results in the decrease of the bearing capacity. Similarly, under the pure-static condition, the slope of the pressure differential of the upper and lower halves of the aerostatic bearings increases with an increase of the radial clearance at the small radial clearance, which results in the increase of the stiffness. However, at the bigger radial clearance, the slope of the pressure differential of the upper and lower halves of the aerostatic bearings decreases with an increase of the radial clearance, which results in the decrease of the stiffness. When the rotational speed is high, the rotational effect weakens with the increase of the radial clearance, which results in the decrease of the stiffness.

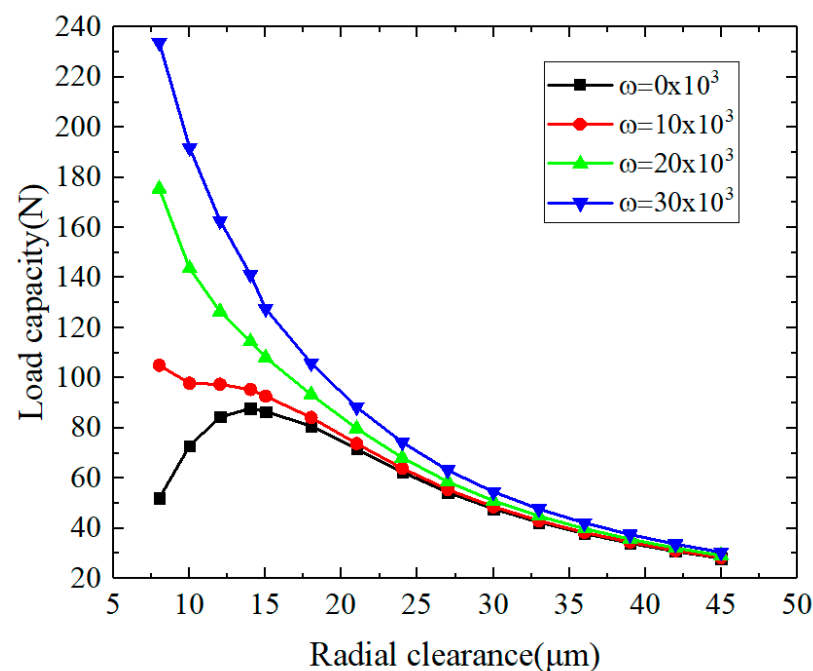


Figure 9. The effects of radial clearance and rotational speed on the load capacity (reference parameters: $d_0 = 0.2$ mm, $p_s = 7$ atm, $\varepsilon = 0.4$).

As shown in Figure 11, the attitude angle decreases with the increase of the radial clearance. When the radial clearance is small, the slope of the attitude angle is big with the change of the radial clearance. Conversely, the slope of attitude angle is small with the change of the radial clearance.

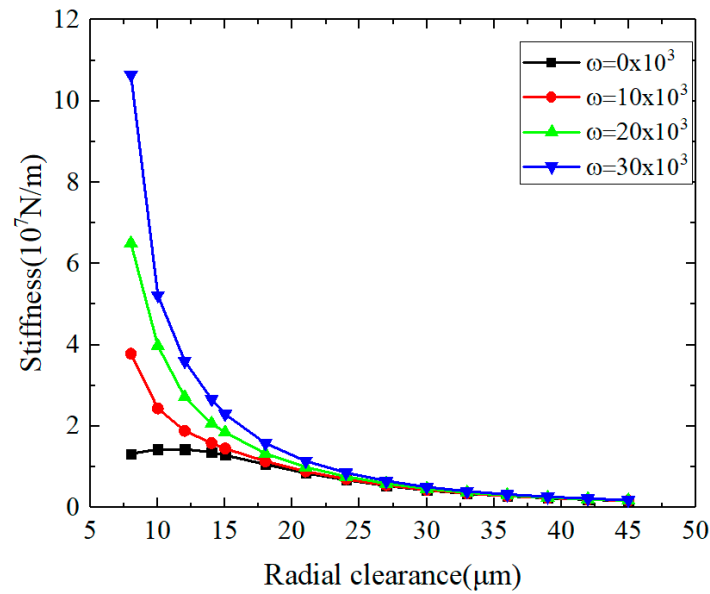


Figure 10. The effects of radial clearance and rotational speed on the steady stiffness (reference parameters: $d_0 = 0.2$ mm, $p_s = 7$ atm, $\varepsilon = 0.4$).

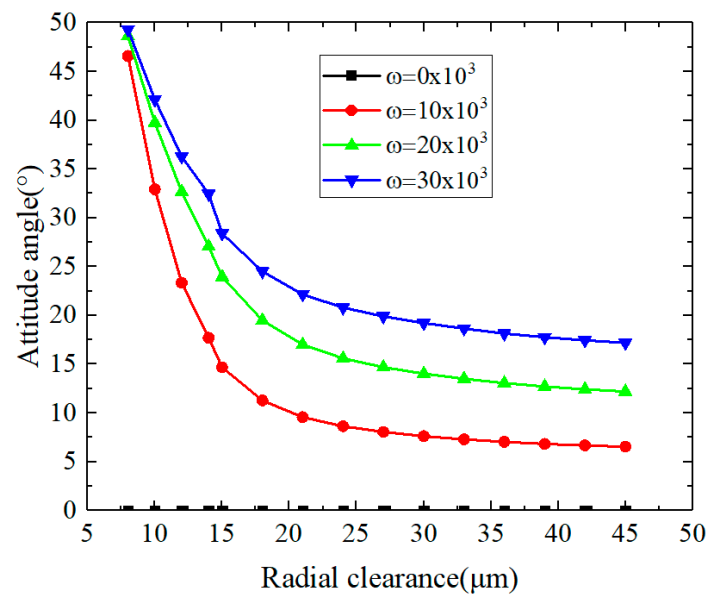


Figure 11. The effects of radial clearance and rotational speed on the attitude angle (reference parameters: $d_0 = 0.2$ mm, $p_s = 7$ atm, $\varepsilon = 0.4$).

3.1.3. The Influences of Orifice Diameter

In this section, the reference parameters are $c = 15$ μm , $p_s = 7$ atm, $\varepsilon = 0.4$ and the variable parameters are the orifice diameter and rotational speed. Figures 12–14 give the effects of the orifice diameter on the bearing capacity, static stiffness and attitude angle. As shown in Figures 12 and 13, whether the aerostatic bearing is under the pure-static or hybrid state, the bearing capacity and stiffness increase first and then decrease with the increase of the orifice diameter. This is combined with the effect of the radial clearance on the static performance in the last section. In the design of the aerostatic bearing, there exists an optimal value for the radial clearance and orifice diameter, which makes its static characteristics reach an optimal result. Moreover, as shown in Figure 14, under a high speed, the attitude angle increases with the increase of the orifice diameter, while the attitude angle decreases with the increase of the orifice diameter under low speed conditions.

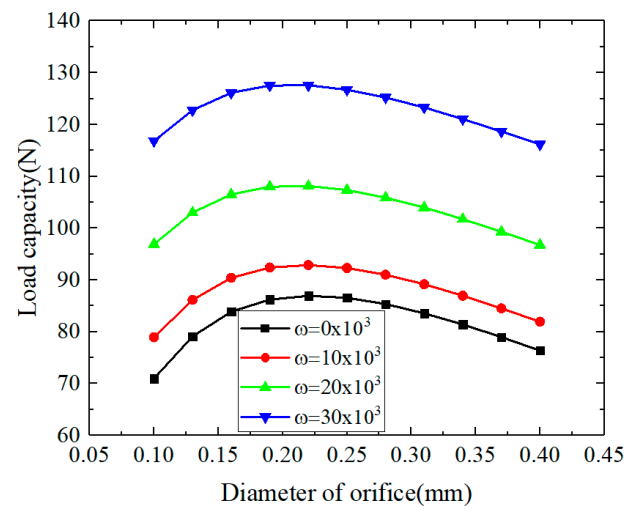


Figure 12. The effects of the diameter of the orifice on the load capacity (reference parameters: $c = 15 \mu\text{m}$, $p_s = 7 \text{ atm}$, $\varepsilon = 0.4$).

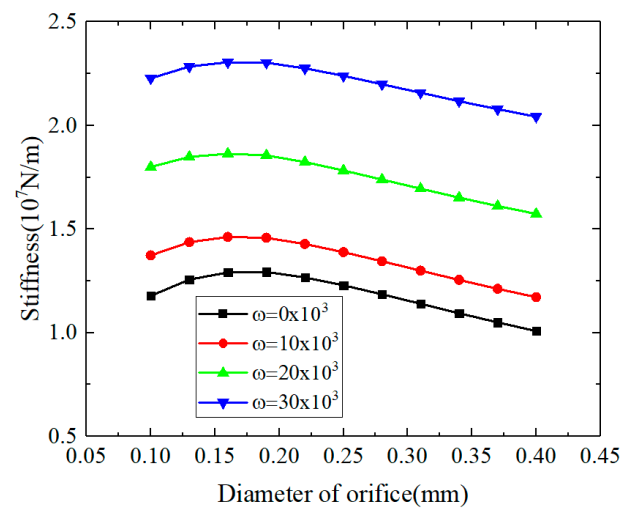


Figure 13. The effects of the diameter of the orifice on the steady stiffness (reference parameters: $c = 15 \mu\text{m}$, $p_s = 7 \text{ atm}$, $\varepsilon = 0.4$).

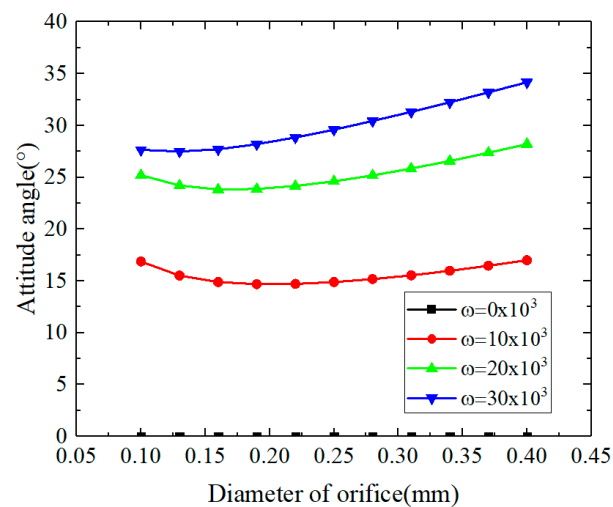


Figure 14. The effects of the diameter of the orifice on the attitude angle (reference parameters: $c = 15 \mu\text{m}$, $p_s = 7 \text{ atm}$, $\varepsilon = 0.4$).

3.1.4. The Influences of Supply Pressure

In this section, the reference parameters are $c = 15 \mu\text{m}$, $d_0 = 0.2 \text{ mm}$, $\varepsilon = 0.4$ and the variable parameters are the supply pressure and rotational speed. Figures 15–17 give the effects of the supply pressure on the bearing capacity, static stiffness and attitude angle. As shown in Figure 15, the bearing capacity and stiffness increase with the increase of the supply pressure. This is because the increase of the external air supply pressure strengthens the static pressure effect of the aerostatic bearing, which increases the bearing capacity and stiffness. Therefore, in order to improve the bearing capacity and static stiffness of the aerostatic gas bearing, the supply pressure can be appropriately increased. However, as the excessive air supply pressure may lead to instability of the air hammer, the supply pressure cannot be too high [34]. As shown in Figure 17, under the hybrid state, the attitude angle decreases with the increase of the supply pressure. Under the pure-static state, the attitude angle is zero. Therefore, the enhanced the supply pressure can strengthen the static pressure effect, which results in the decrease of the attitude angle under the hybrid state.

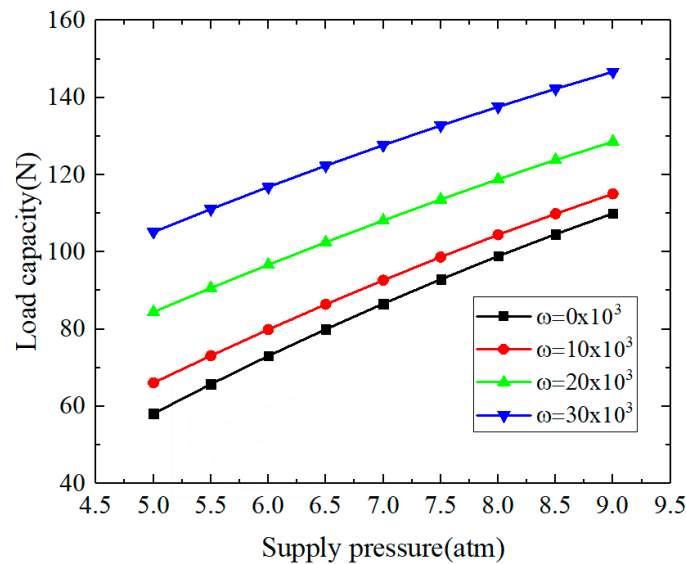


Figure 15. The effects of supply pressure on the load capacity (reference parameters: $c = 15 \mu\text{m}$, $d_0 = 0.2 \text{ mm}$, $\varepsilon = 0.4$).

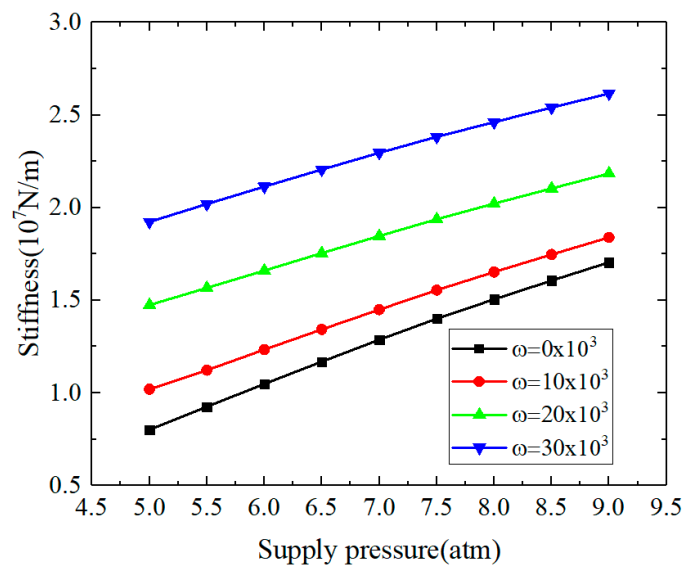


Figure 16. The effects of supply pressure on the steady stiffness (reference parameters: $c = 15 \mu\text{m}$, $d_0 = 0.2 \text{ mm}$, $\varepsilon = 0.4$).

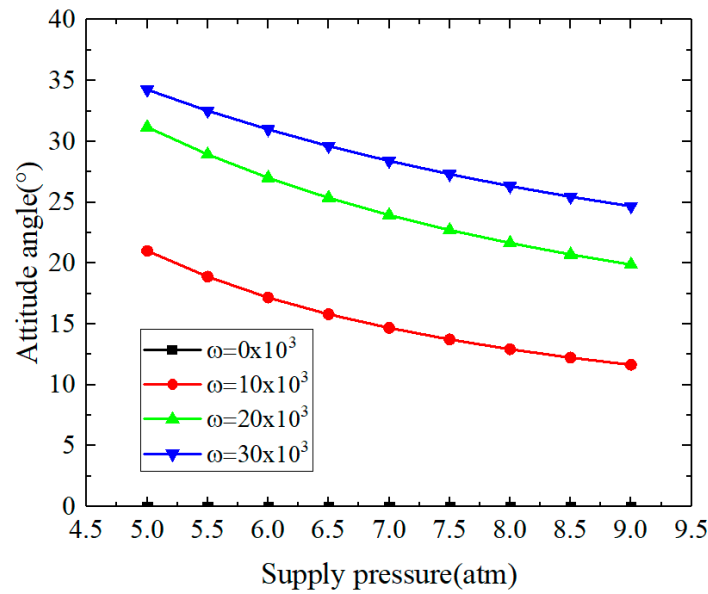


Figure 17. The effects of supply pressure on the attitude angle (reference parameters: $c = 15 \mu\text{m}$, $d_0 = 0.2 \text{ mm}$, $\varepsilon = 0.4$).

3.2. Dynamic Performances

In this section, according to the Section 2 theory and method, the influences of different parameters on the dynamic performances (such as dynamic stiffness, dynamic coefficients, linear stability and so on) are studied as follows. The aerostatic bearings parameters used in this section can be seen in Table 3.

Table 3. The calculation parameters used in this section.

Calculation Parameters	Value
Bearing diameter (D)	50 mm
Bearing length (L)	50 mm
Gas density (ρ)	1.204 kg/m^3
Gas viscosity (η)	$1.82 \cdot 10^{-5} \text{ Ns/m}^2$
Ration of specific heats of gas (κ)	1.4
Atmospheric pressure (atm) (p_a)	101,325 Pa
Rows of the orifice	2
The orifice number of each row orifice	8

3.2.1. Dynamic Coefficients

As shown in Figures 18 and 19, the effect of the rotational speed on the dynamic stiffness and damping coefficients is studied and the reference parameters are $\varepsilon = 0.4$, $d_0 = 0.2 \text{ mm}$, $\lambda = 1$, $c = 15 \mu\text{m}$, $p_s = 7 \text{ atm}$. The bearing principal stiffness coefficients increase with the increase of the rotational speed and the principal stiffness K_{YY} is bigger than the K_{XX} , as shown in Figure 18. The reason is that the rotational effect strengthens with the increase of the speed and leads to the increase of the bearing principal stiffness. Moreover, as the direction of the bearing capacity is vertical, the principal stiffness along the vertical direction K_{YY} is bigger than the principal stiffness along the horizontal direction K_{XX} . Furthermore, the absolute value of the cross-couple stiffness K_{XY} and K_{YX} decreases first and then increases with the increase of the speed. However, the slope of the cross-couple stiffness is smaller than that of the principal stiffness. As shown in Figure 19, the principal damping and cross-couple damping change in the same way with rotational speed, i.e., they decrease first and then increase with an increase of the speed, while the principal damping along the vertical direction C_{YY} is bigger than along the horizontal direction C_{XX} . The reason for this is the same as the bearing principal stiffness.

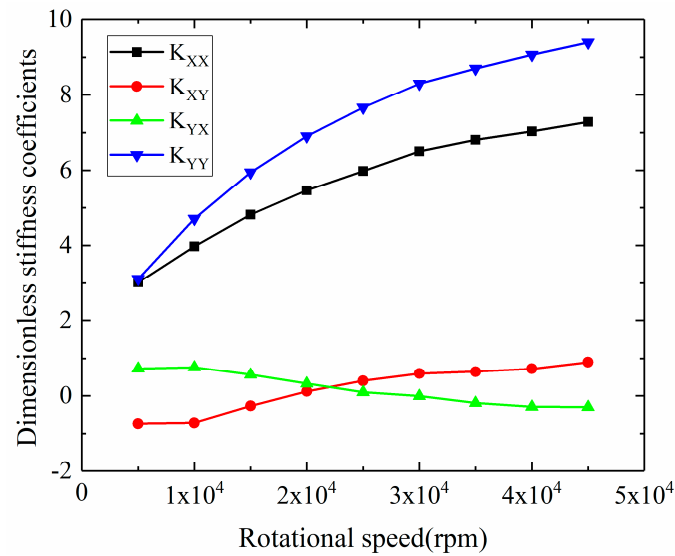


Figure 18. The effect of rotational speed on the dynamic stiffness coefficients (reference parameters: $\varepsilon = 0.4$, $d_0 = 0.2$ mm, $\lambda = 1$, $c = 15$ μm , $p_s = 7$ atm).

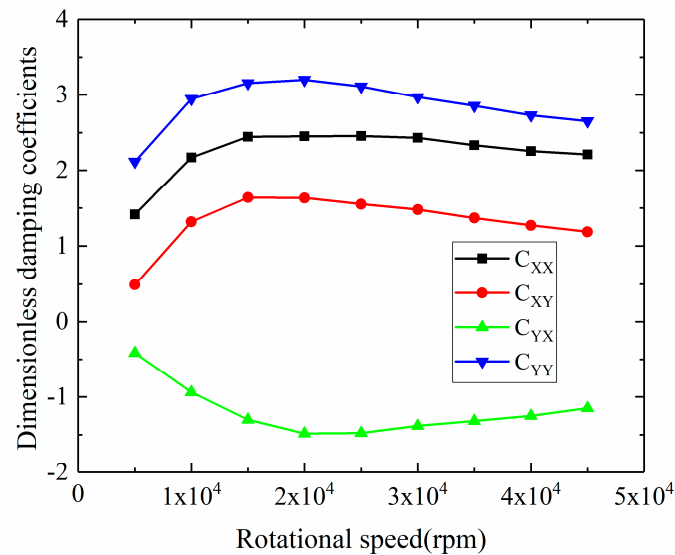


Figure 19. The effect of rotational speed on the damping coefficients (reference parameters: $\varepsilon = 0.4$, $d_0 = 0.2$ mm, $\lambda = 1$, $c = 15$ μm , $p_s = 7$ atm).

As shown in Figures 20 and 21, the effect of the eccentricity on the dynamic stiffness and damping coefficients is studied and the reference parameters are $\omega = 25,000$ rpm, $d_0 = 0.2$ mm, $\lambda = 1$, $c = 15$ μm , $p_s = 7$ atm. As shown in Figure 20, the bearing principal stiffness and slope of the principal stiffness increase with the increase of the eccentricity and the principal stiffness K_{YY} and the slope of it is bigger than that of K_{XX} . The reason is that the rotational effect strengthens with the increase of the eccentricity and leads to the increase of the bearing principal stiffness. Moreover, the rotational effect obviously strengthens at the high eccentricity. Furthermore, the absolute value of the cross-couple stiffness K_{XY} and K_{YX} increases slowly with the increase of the eccentricity. However, the sensitivity of the cross-couple stiffness is weaker than the principal stiffness. As shown in Figure 21, the principal damping and cross-couple damping change in the same way with eccentricity, i.e., they increase with an increase of the eccentricity.

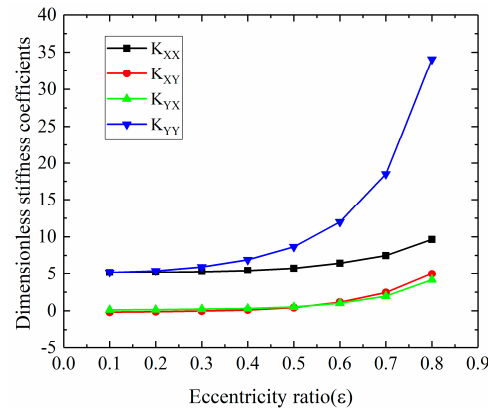


Figure 20. The effect of the eccentricity ratio on the dynamic stiffness coefficients (reference parameters: $\omega = 25,000$ rpm, $d_0 = 0.2$ mm, $\lambda = 1$, $c = 15$ μ m, $p_s = 7$ atm).

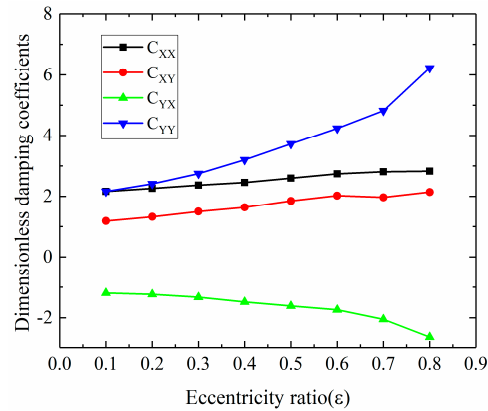


Figure 21. The effect of the eccentricity ratio on the damping coefficients (reference parameters: $\omega = 25,000$ rpm, $d_0 = 0.2$ mm, $\lambda = 1$, $c = 15$ μ m, $p_s = 7$ atm).

As shown in Figures 22 and 23, the effect of the orifice diameter on the dynamic stiffness and damping coefficients is studied and the reference parameters are $\omega = 25,000$ rpm, $\epsilon = 0.4$, $\lambda = 1$, $c = 15$ μ m, $p_s = 7$ atm. The principal stiffness increases and then decreases with the increase of the orifice diameter, while the principal stiffness is not too sensitive to the orifice diameter. The effect of the orifice diameter on the cross-couple stiffness K_{XY} and K_{YX} is opposite, in which the former decreases and the latter increases with the increase of the diameter. As shown in Figure 23, the principal and cross-couple damping enhance with the increase of the orifice diameter.

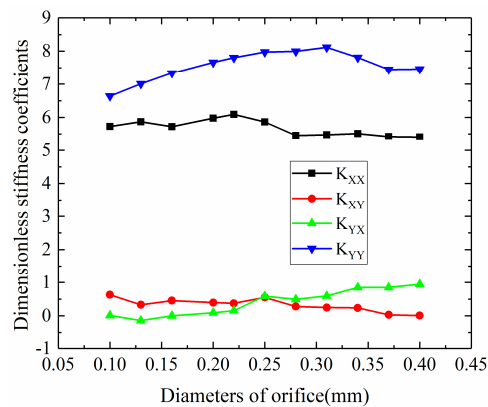


Figure 22. The effect of the diameter of the orifice on the dynamic stiffness coefficients (reference parameters: $\omega = 25,000$ rpm, $\epsilon = 0.4$, $\lambda = 1$, $c = 15$ μ m, $p_s = 7$ atm).

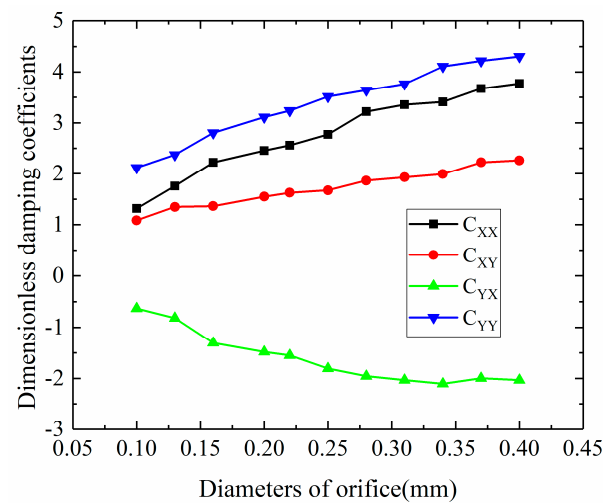


Figure 23. The effect of the diameter of the orifice on the damping coefficients (reference parameters: $\omega = 25,000$ rpm, $\varepsilon = 0.4$, $\lambda = 1$, $c = 15 \mu\text{m}$, $p_s = 7$ atm).

As shown in Figures 24 and 25, the effect of the radial clearance on the dynamic stiffness and damping coefficients is studied and the reference parameters are $\omega = 25,000$ rpm, $d_0 = 0.2$ mm, $\lambda = 1$, $\varepsilon = 0.4$, $p_s = 7$ atm. As shown in the two figures, the principal and cross-couple stiffness and damping coefficients decrease with increase of the radial clearance. As the rotational speed is 25,000 rpm, the aerostatic bearing is under a hybrid state, in which the rotational effect plays the main role in the performances of the aerostatic bearings. The rotational effect will be weakened by increasing the radial clearance, which results in the decrease of the dynamics' coefficients.

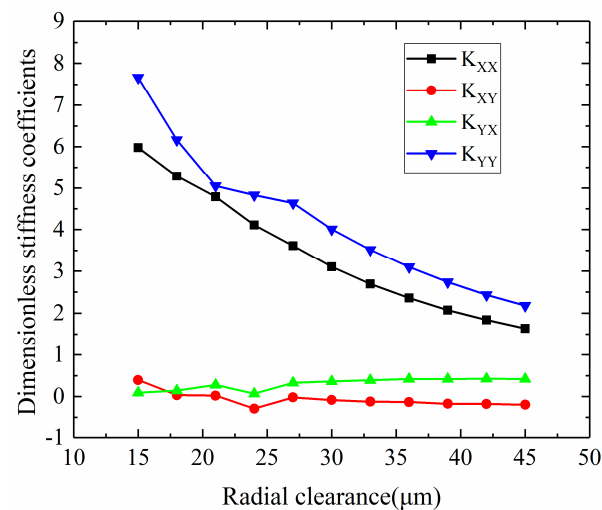


Figure 24. The effect of radial clearance on the dynamic stiffness coefficients (reference parameters: $\omega = 25,000$ rpm, $d_0 = 0.2$ mm, $\lambda = 1$, $\varepsilon = 0.4$, $p_s = 7$ atm).

As shown in Figures 26 and 27, the effect of the supply pressure on the dynamic stiffness and damping coefficients is investigated and the reference parameters are $\omega = 25,000$ rpm, $d_0 = 0.2$ mm, $\lambda = 1$, $\varepsilon = 0.4$, $c = 15 \mu\text{m}$. The static pressure effect is enhanced by increasing the supply pressure and leads to the increase of the principal dynamic coefficients, as shown in Figures 26 and 27. Moreover, the cross-couple dynamic coefficients are not sensitive to the supply pressure.

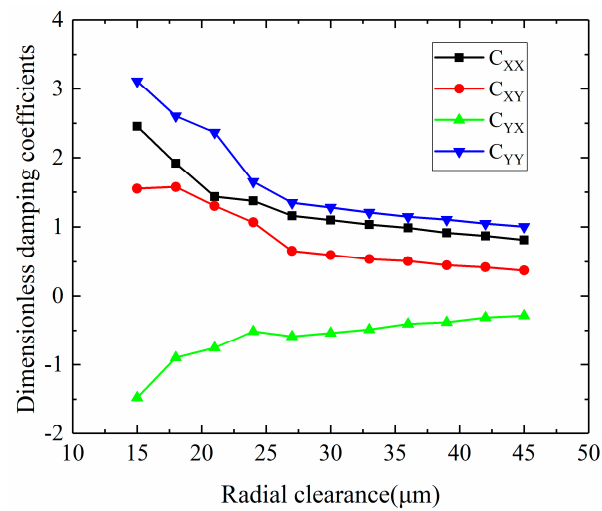


Figure 25. The effect of radial clearance on the damping coefficients (reference parameters: $\omega = 25,000$ rpm, $d_0 = 0.2$ mm, $\lambda = 1$, $\varepsilon = 0.4$, $p_s = 7$ atm).

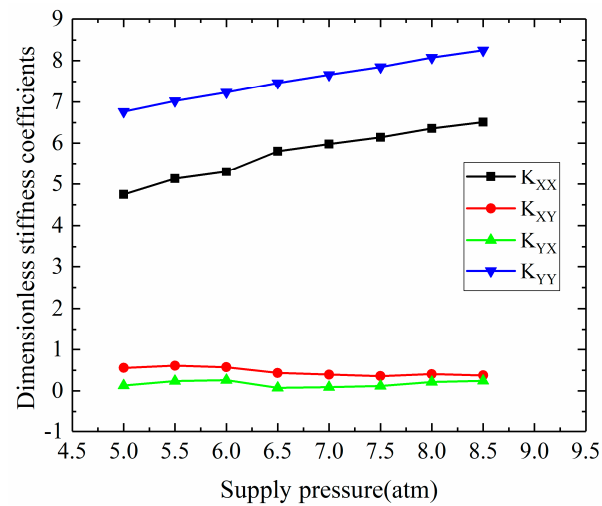


Figure 26. The effect of supply pressure on the dynamic stiffness coefficients (reference parameters: $\omega = 25,000$ rpm, $d_0 = 0.2$ mm, $\lambda = 1$, $\varepsilon = 0.4$, $c = 15$ μm).

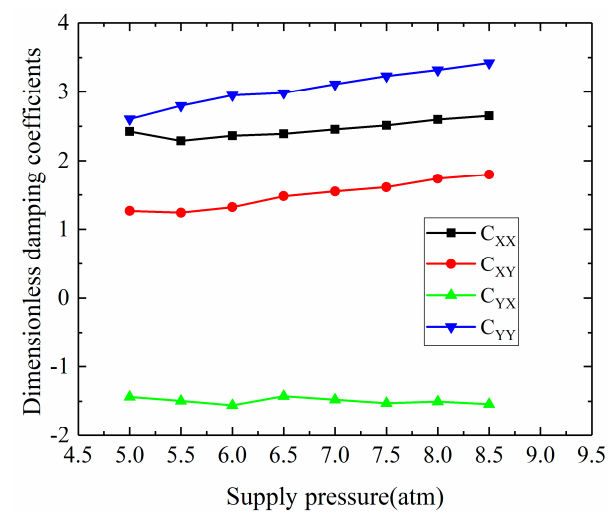


Figure 27. The effect of supply pressure on the damping coefficients (reference parameters: $\omega = 25,000$ rpm, $d_0 = 0.2$ mm, $\lambda = 1$, $\varepsilon = 0.4$, $c = 15$ μm).

As shown in Figures 28 and 29, the effect of the whirl ratio on the dynamic stiffness and damping coefficients is investigated and the reference parameters are $\omega = 25,000$ rpm, $d_0 = 0.2$ mm, $c = 15$ μ m, $\epsilon = 0.4$, $p_s = 7$ atm. As shown in these figures, the dynamic stiffness and damping are sensitivity to the whirl ration. With the increase of the whirl ratio, the principal stiffness increases continuously and finally tends to a constant value. Within the whirl ratio of 0.5~2, the slope of the principal stiffness is obviously higher than that of the other whirl ratio. The principal damping increases and then decreases with the increase of the whirl ratio. In addition, the cross-couple stiffness and damping tend to zero with an increase of the whirl ratio.

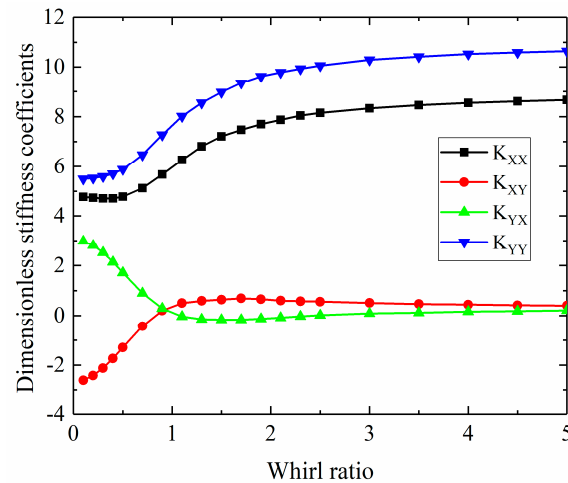


Figure 28. The effect of whirl ratio on the dynamic stiffness coefficients (reference parameters: $\omega = 25,000$ rpm, $d_0 = 0.2$ mm, $c = 15$ μ m, $\epsilon = 0.4$, $p_s = 7$ atm).

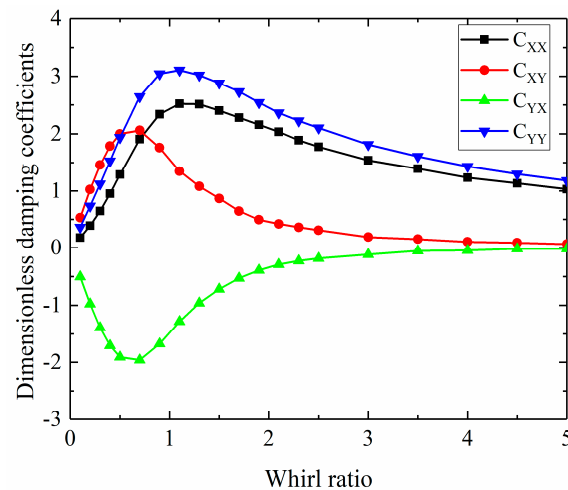


Figure 29. The effect of whirl ratio on the damping coefficients (reference parameters: $\omega = 25,000$ rpm, $d_0 = 0.2$ mm, $c = 15$ μ m, $\epsilon = 0.4$, $p_s = 7$ atm).

3.2.2. Linear Stability of the Gas-Rotor System

As mentioned above, the bearing dynamic stiffness and damping are sensitive to the geometry parameters and supply pressure. According to Equation (27), these parameters affect the linear stability of the aerostatic bearings. In this section, the critical whirl ratio and critical inertial force are used to represent the linear stability of the aerostatic bearing-rotor system.

Based on the study of Section 3.1.1, combined with the motion of the rigid rotor system, the linear stability will be studied by solving Equation (27) in the following. The main

content contains the influence of the eccentricity, rotational speed, supply pressure and radial clearance on the critical whirl ratio and critical inertial force.

The influence of the eccentricity on the critical whirl ratio and critical inertial force under different supply pressure is shown in Figures 30 and 31. As shown in Figure 30, under the lower eccentricity, the critical whirl ratio λ_c is almost equal to 0.5, which is the “half-speed whirl” instability phenomenon. The λ_c decreases with the increase of the eccentricity and the reduction is more obvious under the high eccentricity condition. Furthermore, the λ_c decreases as the supply pressure increases and the decrease of the λ_c with the supply pressure is more obvious under the high eccentricity. As shown in Figure 31, the critical inertial force $(M\lambda^2)_c$ increases with the increase of the eccentricity and the slope of the increase is bigger under the high eccentricity condition. Moreover, for a certain eccentricity, $(M\lambda^2)_c$ increases with the increase of the supply pressure and the slope of the increase is more obvious under the low eccentricity.

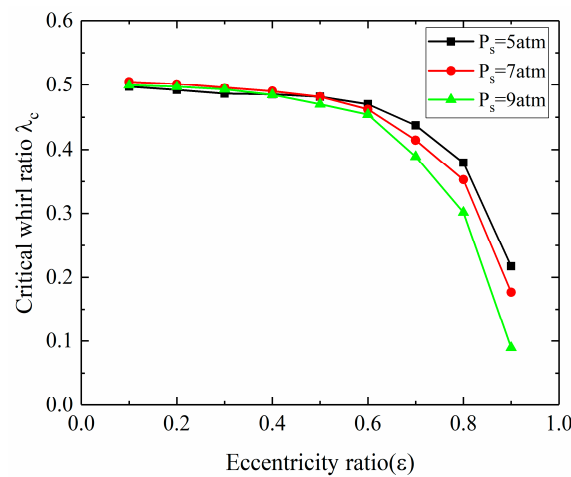


Figure 30. The effect of the eccentricity ratio on the critical whirl ratio.

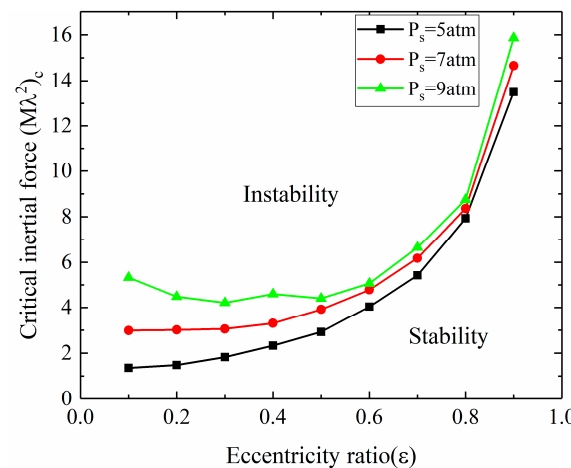


Figure 31. The effect of the eccentricity ratio on the critical inertial force.

As shown in Figures 32 and 33, the influence of the rotational speed on the critical whirl ratio and critical inertial force under different supply pressure is investigated. As shown in Figure 32, the λ_c increases rapidly with the increase of the rotational speed under the low-speed condition and then tends to be a constant value (slightly less than 0.5) under high speed. As shown in Figure 33, the $(M\lambda^2)_c$ also increases with the increase of the speed. Furthermore, the λ_c will be reduced by an increase in the supply pressure and $(M\lambda^2)_c$ will be improved by increased the supply pressure under different rotational speed conditions.

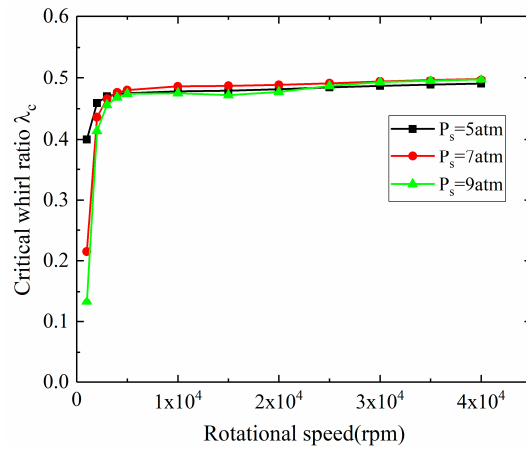


Figure 32. The effect of rotational speed on the critical whirl ratio.

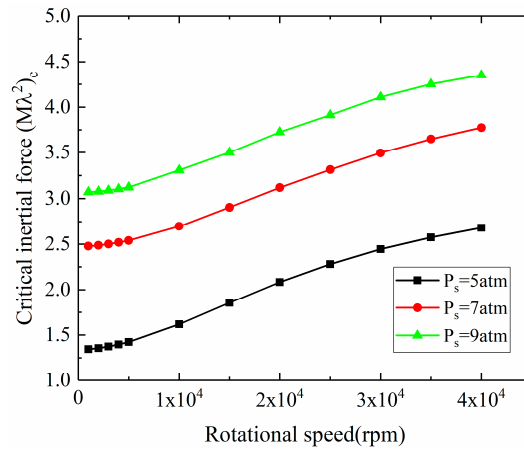


Figure 33. The effect of rotational speed on the critical inertial force.

As shown in Figures 34 and 35, the influence of the radial clearance on the critical whirl ratio and critical inertial force under different supply pressure is investigated. As shown in Figure 34, the λ_c decreases rapidly with the increase of the radial clearance under the low radial clearance condition and the λ_c is not sensitive to the radial clearance under high radial clearance conditions. As shown in Figure 35, the reduces with the increase of the radial clearance. Moreover, the supply pressure can improve the $(M\lambda^2)_c$ and reduce the λ_c under different radial clearance.

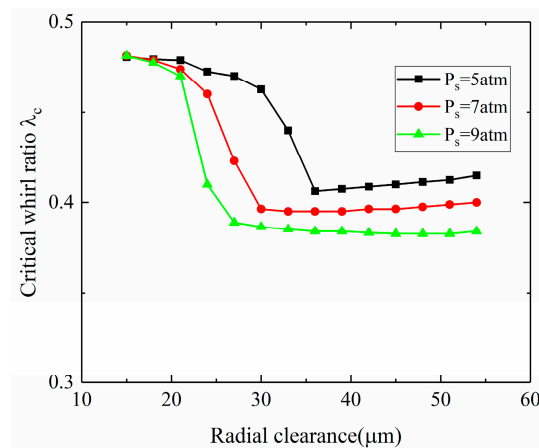


Figure 34. The effect of radial clearance on the critical whirl ratio.

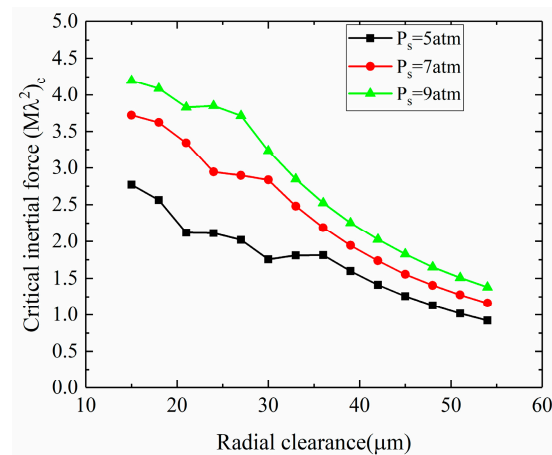


Figure 35. The effect of radial clearance on the critical inertial force.

4. Conclusions

In this paper, the steady state and dynamic Reynolds equation were solved by FDM and the motion equation of a rigid rotor-bearing system was solved to study the linear stability of aerostatic bearings combined with the dynamic coefficients. Based on the theory, the effects of the different parameters on the static and dynamic performances of the aerostatic bearings were studied in detail. The main conclusions shown are as follows:

(1) In the case of the rotational speed effect, when the speed is low (in this paper, the speed is under 10,000 rpm), the static pressure effect plays the main role on the steady performances (such as load capacity and static stiffness), while the rotational effect plays an important role on the steady performances under high speed (in this paper, the speed is over 10,000 rpm).

(2) The whirl ratio plays an important role in the dynamic coefficients. The principal stiffness increases with the increase of the whirl ratio and the cross-couple stiffness tends to be zero with the whirl ratio. Moreover, the principal damping increases first and then decreases with the increase of the whirl ratio. The cross-couple damping also tends to be zero with the increase of the whirl ratio.

(3) As the supply pressure and eccentricity increase, the critical whirl ratio decreases and the critical inertial force increases. The critical whirl ratio and critical inertial force increase with the increase of the rotational speed and the critical whirl ratio tends to 0.5. In addition, the critical whirl ratio increases first and then decreases to a constant with the increase of the radial clearance, while the critical inertial force decreases.

Author Contributions: The author's contributions can be seen in the follows. The contributions of J.Z. are conceptualization and writing—original draft; the contributions of Z.D. is formal analysis; the contributions of K.Z. are formal analysis and methodology; the contributions of H.J. is funding acquisition; the contributions of T.Y. are investigation and methodology; the contributions of Z.S. is investigation; the contributions of C.C. is formal analysis; the contributions of Y.C. is formal analysis; the contributions of Z.X. and D.W. are formal analysis and investigation; the contributions of J.S. is writing—review & editing. All authors have read and agreed to the published version of the manuscript.

Funding: The present research has been funded by the National Science and Technology Major Project of China (J2019-IV-0005-0072 and 2017-I-0008-0009); the authors would like to sincerely express their appreciation.

Data Availability Statement: The datasets used and/or analyzed during the current study are available from the corresponding author upon reasonable request.

Conflicts of Interest: The authors declare no conflict of interest.

Nomenclature

c	radial clearance	p_a, P_a	ambient pressure
C_d	discharge coefficient	p_s, P_s	supply gauge pressure
d_0	diameter of orifices	R	radius of journal bearing
D	diameter of journal bearing	t, τ	time, dimensionless time
e	eccentricity	u	circumferential velocity
A_0, B_0, C_0, D_0, E_0	coefficient matrices in	w	axial velocity
A_X, B_X, C_X, D_X, E_X	solution of Reynolds equation	W	load capacity
$k_{xx}, k_{xy}, k_{yx}, k_{yy}$	dynamic coefficients	x, X	circumferential coordinate
$c_{xx}, c_{xy}, c_{yx}, c_{yy}$	dimensionless dynamic coefficients	y, Y	radial coordinate
$K_{xx}, K_{xy}, K_{yx}, K_{yy}$	static stiffness	z, Z	axial coordinate
$C_{xx}, C_{xy}, C_{yx}, C_{yy}$	dimensionless static stiffness	ε	eccentricity ratio, $\varepsilon = e/c$
K_w	inertial force	ρ, ρ_a	gas density and gas density under atmosphere pressure
k_{eq}	dimensionless inertial force	ω	rotational speed of journal
K_{eq}	film thickness, $H = h/c$	ω_s	journal perturbation rotational speed
h, H	length of the bearing	λ	whirl ratio
L	differential term of film thickness	Λ	bearing number
H_X, H_Y	rigid rotor mass	φ_0	attitude angle
m_r	dimensionless rotor mass	κ	ratio of specific heats of gas
\bar{M}	dimensionless mass flow rate at rth orifice	δ	Kronecker function
Q_r	differential term of dimensionless mass flow rate at rth orifice	$i, i - 1, i + 1,$ $j, j - 1, j + 1$	the subscript along circumference and axial direction, which indicates the position of the pressure
Q_{rX}, Q_{rY}	mass flow rate at rth orifice	subscript c	the critical parameters
p	gas pressure	$\dot{x}, \ddot{x}, \dot{y}, \ddot{y}$	velocity and acceleration along X and Y direction
P_0	the dimensionless steady pressure		
P_X, P_Y	differential term of film pressure		

Appendix A

$$Q_{rX} = \begin{cases} \Gamma_s p_s C_d \sqrt{\frac{2\rho_a}{p_a}} \pi d_0 c \left(\frac{2}{\kappa+1}\right)^{\frac{\kappa}{\kappa-1}} H_{Xij}; \text{ if } \frac{p_{0rij}}{p_s} \leq \left(\frac{2}{\kappa+1}\right)^{\frac{\kappa}{\kappa-1}} \\ \Gamma_s p_s C_d \sqrt{\frac{2\rho_a}{p_a}} \pi d_0 c \sqrt{\frac{\kappa}{\kappa-1}} \left\{ H_X \sqrt{\left(\frac{p_{0rij}}{P_s}\right)^{\frac{2}{\kappa}} - \left(\frac{p_{0ij}}{P_s}\right)^{\frac{\kappa+1}{\kappa}}} + \frac{H_0 \left[\frac{2}{\kappa} \left(\frac{p_{0rij}}{P_s}\right)^{\frac{2}{\kappa-1}} \frac{1}{P_s} - \frac{\kappa+1}{\kappa} \left(\frac{p_{0rij}}{P_s}\right)^{\frac{1}{\kappa}} \frac{1}{P_s} \right]}{2 \sqrt{\left(\frac{p_{0rij}}{P_s}\right)^{\frac{2}{\kappa}} - \left(\frac{p_{0ij}}{P_s}\right)^{\frac{\kappa+1}{\kappa}}}} \right\}; \\ \text{if } \frac{p_{0rij}}{p_s} > \left(\frac{2}{\kappa+1}\right)^{\frac{\kappa}{\kappa-1}} \end{cases}$$

$$Q_{rY} = \begin{cases} \Gamma_s p_s C_d \sqrt{\frac{2\rho_a}{p_a}} \pi d_0 c \left(\frac{2}{\kappa+1}\right)^{\frac{\kappa}{\kappa-1}} H_{Yij}; \text{ if } \frac{p_{0rij}}{p_s} \leq \left(\frac{2}{\kappa+1}\right)^{\frac{\kappa}{\kappa-1}} \\ \Gamma_s p_s C_d \sqrt{\frac{2\rho_a}{p_a}} \pi d_0 c \sqrt{\frac{\kappa}{\kappa-1}} \left\{ H_Y \sqrt{\left(\frac{p_{0rij}}{P_s}\right)^{\frac{2}{\kappa}} - \left(\frac{p_{0ij}}{P_s}\right)^{\frac{\kappa+1}{\kappa}}} + \frac{H_0 \left[\frac{2}{\kappa} \left(\frac{p_{0rij}}{P_s}\right)^{\frac{2}{\kappa-1}} \frac{1}{P_s} - \frac{\kappa+1}{\kappa} \left(\frac{p_{0rij}}{P_s}\right)^{\frac{1}{\kappa}} \frac{1}{P_s} \right]}{2 \sqrt{\left(\frac{p_{0rij}}{P_s}\right)^{\frac{2}{\kappa}} - \left(\frac{p_{0ij}}{P_s}\right)^{\frac{\kappa+1}{\kappa}}}} \right\}; \\ \text{if } \frac{p_{0rij}}{p_s} > \left(\frac{2}{\kappa+1}\right)^{\frac{\kappa}{\kappa-1}} \end{cases}$$

References

- Zhang, J.; Zou, D.; Ta, N.; Rao, Z. Numerical research of pressure depression in aerostatic thrust bearing with inherent orifice. *Tribol. Int.* **2018**, *123*, 385–396. [CrossRef]
- Zhang, J.; Zou, D.; Ta, N.; Rao, Z.; Ding, B. A numerical method for solution of the discharge coefficients in externally pressurized gas bearings with inherent orifice restrictors. *Tribol. Int.* **2018**, *125*, 156–168. [CrossRef]

3. Dal, A.; Karaçay, T. Effects of angular misalignment on the performance of rotor-bearing systems supported by externally pressurized air bearing. *Tribol. Int.* **2017**, *111*, 276–288. [[CrossRef](#)]
4. Zhu, X.; San Andrés, L. Rotordynamic Performance of Flexure Pivot Hydrostatic Gas Bearings for Oil-Free Turbomachinery. *J. Eng. Gas Turbines Power* **2007**, *129*, 1020–1027. [[CrossRef](#)]
5. Zhang, J.; Han, D.; Song, M.; Xie, Z.; Zou, D. Theoretical and experimental investigation on the effect of supply pressure on the nonlinear behaviors of the aerostatic bearing-rotor system. *Mech. Syst. Signal Process.* **2021**, *158*, 107775. [[CrossRef](#)]
6. Zhang, J.; Han, D.; Xie, Z.; Huang, C.; Su, Z. Nonlinear behaviors analysis of high-speed rotor system supported by aerostatic bearings. *Tribol. Int.* **2022**, *170*, 107111. [[CrossRef](#)]
7. Qiu, Z.; Tieu, A. Misalignment effect on the static and dynamic characteristics of hydrodynamic journal bearings. *J. Tribol.* **1995**, *117*, 717–723. [[CrossRef](#)]
8. Lahmar, M.; Frihi, D.; Nicolas, D. The effect of misalignment on performance characteristics of engine main crankshaft bearings. *Eur. J. Mech.-A/Solids* **2002**, *21*, 703–714. [[CrossRef](#)]
9. Lv, F.; Rao, Z.; Ta, N.; Jiao, C. Mixed-lubrication analysis of thin polymer film overlaid metallic marine stern bearing considering wall slip and journal misalignment. *Tribol. Int.* **2017**, *109*, 390–397. [[CrossRef](#)]
10. Lv, F.; Jiao, C.; Ta, N.; Rao, Z. Mixed-lubrication analysis of misaligned bearing considering turbulence. *Tribol. Int.* **2018**, *119*, 19–26. [[CrossRef](#)]
11. Wrblewski, P.; Iskra, A. Geometry of shape of profiles of the sliding surface of ring seals in the aspect of friction losses and oil film parameters. *Combust. Engines* **2016**, *167*, 38–52. [[CrossRef](#)]
12. Rostek, E.; Babiak, M.; Wróblewski, E. The Influence of Oil Pressure in the Engine Lubrication System on Friction Losses. *Procedia Eng.* **2017**, *192*, 771–776. [[CrossRef](#)]
13. Chen, C.-H.; Kang, Y.; Yang, D.-W.; Hwang, R.-M.; Shyr, S.-S. Influence of the number of feeding holes on the performances of aerostatic bearings. *Ind. Lubr. Tribol.* **2010**, *62*, 150–160. [[CrossRef](#)]
14. Ise, T.; Miyatake, H.; Asami, T. Asymmetric Supply Type Hydrostatic Journal Gas Bearings to Support Large Load Rotors. *J. Adv. Mech. Des. Syst. Manuf.* **2012**, *6*, 149–157. [[CrossRef](#)]
15. Du, J.; Zhang, G.; Liu, T.; To, S. Improvement on load performance of externally pressurized gas journal bearings by opening pressure-equalizing grooves. *Tribol. Int.* **2014**, *73*, 156–166. [[CrossRef](#)]
16. Su, J.C.; Lie, K. Rotation effects on hybrid air journal bearings. *Tribol. Int.* **2003**, *36*, 717–726. [[CrossRef](#)]
17. Yang, D.-W.; Chen, C.-H.; Kang, Y.; Hwang, R.-M.; Shyr, S.-S. Influence of orifices on stability of rotor-aerostatic bearing system. *Tribol. Int.* **2009**, *42*, 1206–1219. [[CrossRef](#)]
18. Wang, X.; Xu, Q.; Wang, B.; Zhang, L.; Yang, H.; Peng, Z. Numerical Calculation of Rotation Effects on Hybrid Air Journal Bearings. *Tribol. Trans.* **2017**, *60*, 195–207. [[CrossRef](#)]
19. Wang, X.; Xu, Q.; Wang, B.; Zhang, L.; Yang, H.; Peng, Z. Effect of surface waviness on the static performance of aerostatic journal bearings. *Tribol. Int.* **2016**, *103*, 394–405. [[CrossRef](#)]
20. Lund, J. A theoretical analysis of whirl instability and pneumatic hammer for a rigid rotor in pressurized gas journal bearings. *ASME J. Lubr. Technol.* **1967**, *89*, 154–166. [[CrossRef](#)]
21. Wadhwa, S.; Sinhasan, R.; Singh, D. Analysis of orifice compensated externally pressurized gas bearings. *Tribol. Int.* **1983**, *16*, 203–211. [[CrossRef](#)]
22. Han, D.-C.; Park, S.-S.; Kim, W.-J.; Kim, J.-W. A study on the characteristics of externally pressurized air bearings. *Precis. Eng.* **1994**, *16*, 164–173. [[CrossRef](#)]
23. Su, J.C.; Lie, K. Rotor dynamic instability analysis on hybrid air journal bearings. *Tribol. Int.* **2006**, *39*, 238–248. [[CrossRef](#)]
24. Chen, C.-H.; Yang, D.-W.; Kang, Y.; Hwang, R.-M.; Shyr, S.-S. The influence of orifice restriction on the stability of rigid rotor-aerostatic bearing system. In Proceedings of the ASME Turbo Expo 2009: Power for Land, Sea, and Air, Orlando, FL, USA, 8–12 June 2009; pp. 909–917.
25. Chen, C.-H.; Tsai, T.-H.; Yang, D.-W.; Kang, Y.; Chen, J.-H. The comparison in stability of rotor-aerostatic bearing system compensated by orifices and inferences. *Tribol. Int.* **2010**, *43*, 1360–1373. [[CrossRef](#)]
26. Morosi, S.; Santos, I.F. On the modelling of hybrid aerostatic-gas journal bearings. *Proc. Inst. Mech. Eng. Part J J. Eng. Tribol.* **2011**, *225*, 641–653. [[CrossRef](#)]
27. Colombo, F.; Raparelli, T.; Viktorov, V. Externally pressurized gas bearings: A comparison between two supply holes configurations. *Tribol. Int.* **2009**, *42*, 303–310. [[CrossRef](#)]
28. Otsu, Y.; Somaya, K.; Yoshimoto, S. High-speed stability of a rigid rotor supported by aerostatic journal bearings with compound restrictors. *Tribol. Int.* **2011**, *44*, 9–17. [[CrossRef](#)]
29. Belforte, G.; Raparelli, T.; Viktorov, V. Modeling and identification of gas journal bearings: Self-acting gas bearing results. *Trans.-Am. Soc. Mech. Eng. J. Tribol.* **2002**, *124*, 716–724. [[CrossRef](#)]
30. Viktorov, V.; Belforte, G.; Raparelli, T. Modeling and Identification of Gas Journal Bearings: Externally Pressurized Gas Bearing Results. *J. Tribol.* **2005**, *127*, 548–556. [[CrossRef](#)]
31. Wang, X.; Xu, Q.; Huang, M.; Zhang, L.; Peng, Z. Effects of journal rotation and surface waviness on the dynamic performance of aerostatic journal bearings. *Tribol. Int.* **2017**, *112*, 1–9. [[CrossRef](#)]
32. Xie, Z.; Jiao, J.; Yang, K. Theoretical and experimental study on the fluid-structure-acoustic coupling dynamics of a new water lubricated bearing. *Tribol. Int.* **2023**, *177*, 107982. [[CrossRef](#)]

33. SHINICHI. *Gas Bearing: Design, Fabrication and Application*; Aerospace Publishing House: Beijing, China, 1988.
34. Ma, W.; Cui, J.; Liu, Y.; Tan, J. Improving the pneumatic hammer stability of aerostatic thrust bearing with recess using damping orifices. *Tribol. Int.* **2016**, *103*, 281–288. [[CrossRef](#)]

Disclaimer/Publisher's Note: The statements, opinions and data contained in all publications are solely those of the individual author(s) and contributor(s) and not of MDPI and/or the editor(s). MDPI and/or the editor(s) disclaim responsibility for any injury to people or property resulting from any ideas, methods, instructions or products referred to in the content.